[AMERICAN JOURNAL OF SCIENCE, VOL. 294, JUNE, 1994, P. 713–755]

# NONLINEAR DYNAMICAL ASPECTS OF DEEP BASIN HYDROLOGY: FLUID COMPARTMENT FORMATION AND EPISODIC FLUID RELEASE

T. DEWERS* and P. ORTOLEVA**
Department of Geological Sciences,
Indiana University,
Bloomington, Indiana 47405

**ABSTRACT.** **The notion of abnormally pressured fluid or "pressure" compartments is a new concept associated with sedimentary basins and has implications for petroleum formation and transport, mineralization accompanying fluid explusion from great depths, and overall basin hydrology. In this paper, the coupling between fluid mass conservation, time-dependent compaction, water-rock reaction, and natural hydrofracturing is explored in the context of fluid compartment genesis and preservation during sediment burial. Focus is placed upon examining the complexity associated with this coupling between hydrological, geochemical, and structural factors associated with sedimentary basin development. A natural consequence of at least the early stages of compartment evolution is found to be the episodic (and possibly chaotic) release of fluid to shallow portions of the basin.**

**A simple topological analysis of nonlinearly coupled differential equations for fluid pressure production and dissipation (through a top seal bounding a fluid compartment) and seal hydrofracturing suggests a variety of dynamical phenomena including steady unfractured-states, steady fractured-states, and oscillatory fluid expulsion through a seal accompanying cyclic fracture growth and healing. A quantitative reaction-transport-mechanical model is developed which co-evolves in time and space the variables of fluid pressure and chemical composition, cement content, porosity, and fracture radius, density and aperture. An often-ignored facet of basin evolution is the role of time-dependent processes, such as solution-transfer or pressure solution, in altering porosity and permeability. Although operating on longer time scales than poro-elastic compression accompanying sediment loading, time-dependent compaction offers a larger potential for generating fluid overpressures and plays an integral role in the development of the variety of dynamical states discussed herein. One-dimensional numerical solutions of the model equations simulate generation of abnormal fluid pressures and show consequences of hydrofracturing if overpressure exceeds a critical level. Fluid pressure within overpressured domains may oscillate accompanying hydrofracture-related fluid expulsion and slow build-up with compactional pore volume loss and thermal expansion of pore fluid.**

**One example basinal scenario revealed by simulations involves, upon the initiation of hydrofracturing, a transient phase of oscillatory fluid release, followed by a steady fractured-state reflecting a balance between rates of fracture growth and healing and fluid pressure production and dissipation. The upper boundary of the hydrofractured zone (a**

* Present address: The University of Oklahoma, 810 Sarkeys Energy Center, 100 E. Boyd Street, Norman, Oklahoma 73019-0628.
** Also: Department of Chemistry, Indiana University, Bloomington, Indiana 47405.

**low permeability zone or seal), upon achieving this steady state, undergoes dynamic readjustment with subsidence, occupying a fixed position in depth and forming a moving "front" in the rock-fixed reference frame. Tops of geopressured zones buried several kilometers in actively subsiding basins may follow a similar dynamic, remaining at a constant elevation. Changes in character of fluid explusion from overpressured domains depend on variations in burial rate, the functional relationship between rock texture and permeability, and magnitude of lateral stress.**

SYMBOLS

| | |
|---|---|
| $a$ | mean fracture aperture (cm) |
| $A_c$ | area of puncture in top seal |
| $A_i$ | area of grain surface of type i, i = x, y, z, f; x, y, and z denote contact normal to x, y, z direction, f denotes free-face area ($cm^2$) |
| $b$ | standard deviation of asperity height distribution within fracture (cm) |
| $c$ | molar concentration of solute in pore fluid ($mol/cm^3$) |
| $\bar{c}(p, T)$ | concentration of solute in pore fluid in equilibrium with solid at pressure p and temperature T |
| $c_f^{eq}$ | concentration of solute in pore fluid at equilibrium with grain free faces |
| $\underset{\equiv}{C}$ | elastic compliance tensor of drained porous medium |
| $D$ | diffusion coefficient of solute in water multiplied by sediment tortuosity factor ($cm^2/s$) |
| $D'$ | diffusion coefficient of solute in thin aqueous film within grain-grain contacts multiplied by film width ($cm^3/s$) |
| $E$ | Young's modulus of rock surrounding fracture |
| $E_f$ | activation energy for fracture growth/healing kinetics (ergs/mol) |
| $F$ | rate of change of fracture radius due to growth or healing (cm/s) |
| $G_i$ | rate of change of $L_i$ due to reaction (cm/s) |
| $J$ | flux of solute ($mols/cm^2 \cdot s$) |
| $L$ | thickness of compartment top seal |
| $L_i$ | variables characterizing grain geometry (cm; i = f, z, and x, y denote grain radius, height, and grain width, respectively) |
| $n$ | number of grains per rock volume ($cm^{-3}$) |
| $p$ | fluid pressure (dyn/$cm^2$ or bars) |
| $p_c$ | fluid pressure within a compartment (dyn/$cm^2$ or bars) |
| $p_f$ | fluid pressure in compartment needed to fracture the top seal (dyn/$cm^2$ or bars) |
| $p_h$ | compartment pressure below which fractures in top seal will heal (dyn/$cm^2$ or bars) |
| $p_o$ | fluid pressure above a seal (dyn/$cm^2$ or bars) |
| $\bar{p}$ | reference pressure (dyn/$cm^2$ or bars) |

| | |
|---|---|
| $P_z$ | normal stress at horizontal grain contact (dyn/cm$^2$ in bars) |
| $\vec{q}$ | volume flux of fluid (cm$^3$/cm$^2$ · s) |
| Q | critical energy required for propagation as in eq (11) |
| r | radius of penny-shaped fracture (cm) |
| R | gas constant |
| t | time (s) |
| T | temperature (Kelvin) |
| $\overline{T}$ | reference temperature (Kelvin) |
| $\vec{u}$ | rock flow velocity (cm/s) |
| U | factor relating to energy balance for fracture propagation |
| v′ | parameter in fracture rate expression (15) |
| $\vec{v}$ | velocity of fluid (cm/s) |
| $v_f$ | limiting velocity of fracture growth or healing (cm/s) |
| V | molar volume of solid containing the (nascent) fracture |
| $V_c$ | compartment volume (cm$^3$) |
| $w_i$ | component of macroscopic elastic displacement vector (i = x, y, z) |
| $\alpha$ | coefficient of fluid thermal expansivity (Kelvin$^{-1}$) |
| $\alpha^m$ | effective stress coefficient (dimensionless) |
| $\beta$ | coefficient of fluid compressibility (cm$^2$/dyn) |
| $\Gamma_f$ | fluid mass density multiplied by gravitational acceleration (g/cm · s) |
| $\Gamma_s$ | mass density of sediment solids multiplied by gravitational acceleration (g/cm · s) |
| $\tilde{\Gamma}$ | quantity defined in eq (6) |
| $\delta_{ij}$ | Kronecker delta (=1 for i = j, =0 for i ≠ j) |
| $\Delta$ | mass density of fluid (g/cm$^3$) |
| $\epsilon^m$ | macroscopic (elastic) strain tensor |
| $\eta$ | fracture density (# of fractures/volume, cm$^{-3}$) |
| $\kappa$ | permeability (cm$^2$) |
| $\kappa_s$ | permeability of seal bounding a compartment (cm$^2$) |
| $\kappa^*$ | sum of fracture and matrix permeabilities as defined in eq (22) (cm$^2$) |
| $\lambda^m$ | Lame's constant of drained porous framework (cm$^2$/dyn) |
| $\Lambda$ | quantity defined in eq (6) |
| $\mu$ | fluid viscosity (Poise) |
| $\mu^m$ | shear modulus of porous framework (cm$^2$/dyn) |
| $\nu$ | Poisson's ratio of rock surrounding fracture |
| $\xi$ | normalized depth (dimensionless) |
| $\rho$ | molar density of water (mols/cm$^3$) |
| $\rho_s$ | molar density of solid (mols/cm$^3$) |
| $\overline{\rho}$ | fluid molar density at reference state $\overline{p}$, $\overline{T}$ (mols/cm$^3$) |
| $\sigma_\Gamma$ | far field tensile stress, oriented parallel to the direction of the least compressive stress (dyn/cm$^2$) |
| $\underline{\underline{\sigma}}^m$ | macroscopic stress tensor (components are in dyn/cm$^2$) |
| $\sigma^m_{xx}$ | horizontal component of macroscopic stress tensor; coincides with least principal compressive stress |
| $\phi$ | porosity of bulk rock |

| | |
|---|---|
| $\phi_c$ | porosity within compartment |
| $\phi_f$ | fracture porosity |
| $\phi_m$ | matrix porosity |
| $\phi_w$ | "Weyl" porosity, that is, porosity of porous framework composed of grains in simple cubic packing, after Weyl (1959) |
| $\psi$ | piezometric fluid pressure (dyn/cm$^2$) |
| $\Omega$ | area of top seal as in eq. (3) |
| $d\vec{\Omega}$ | incremental surface area of top seal multiplied by unit inward pointing normal vector |

## INTRODUCTION

The coupling of reaction, transport, and mechanical processes operating during diagenesis in deep sedimentary basins can lead to complex dynamical behavior of rock/fluid systems. Fluid motion within basins can be episodic in time and highly focused in space. At depth basins can subdivide into hydraulically isolated fluid compartments (see companion paper by Ortoleva, Al-Shaieb, and Puckette, in press). In an attempt to describe some of these basin features, a continuum dynamical model is constructed around the interrelated physico-chemical processes of (chemical) compaction, cementation, fluid pressure generation and dissipation, fracture propagation and healing, and solute transport. Simple limiting cases are examined that illustrate the existence of nonlinear dynamical phenomena including episodic fluid flow generated from abnormally pressured zones undergoing hydrofracturing in the deeper portions of sedimentary basins. A transition from steady-state to temporally oscillatory flow with change in subsidence rate is illustrated. One scenario brought out by computer simulation is a two-phase basin history during sediment burial and compaction: an early phase involves generation of abnormal fluid pressures, hydrofracturing, and an initial transient episodic fluid release from an evolving zone of hydrofractures. In the second phase, this gradually evolves to a steady fracturing state wherein a delicate balance is achieved between fluid pressure generation, fluid explusion, and fracture growth and healing.

Episodic fluid release involving a cyclic build-up of overpressure, hydrofracturing, fluid flow and pressure dissipation, fracture healing or sealing, and again overpressuring was proposed as a potential means for hydrocarbon migration by Momper (1978) and Mandl and Harness (1987). Cyclic fluid release from overpressured zones was suggested by Bradley (1975) and is discussed by Cathles (1989) and Walder and Nur (1984) in the context of fracture growth and healing. A simple quantitative model of this phenomenon was presented by Ghaith, Chen, and Ortoleva (1990; see also Chen and others, 1990).

Fluid compartments are large domains of rock hydraulically isolated from their surroundings on all sides by seals; they consequently contain fluids that may be abnormally pressured (that is, fluid pressure which departs from that arising from the weight of the overlying water column). The widespread existence of fluid compartments in most of the world's basins has been postulated by Powley and Bradley (Bradley, 1975;

Powley, 1980, 1990; Dewers and Ortoleva, 1988; Hunt, 1990; Weedman, Guber, and Engelder, 1992; Ortoleva, Al-Shaieb, and Puckette, in press) and is a topic of current interest from aspects of both basin hydrology and migration and trapping of petroleum. The formation and preservation of abnormally pressured zones within deep portions of sedimentary basins quite possibly are fundamental aspects of episodic fluid release to shallower zones; this paper considers the two from a united perspective.

Evidence for episodic fluid release comes from many sources but is largely circumstantial. Perhaps the most conclusive evidence comes from geochemical studies of ore deposits and fluid inclusion analysis. For example, Prikryl, Posey, and Kyle (1988) document five petrographically distinguishable generations of calcite cement in cap rock from Damon Mound salt dome, Texas, each relating isotopically to a distinct fluid flow event. Cathles and Smith (1983) argue that formation of Mississippi Valley-type ore deposits requires both the higher temperatures and higher velocities characteristic of a pulsatile fluid release from deeper portions of sedimentary basins. Physical evidence for episodic fluid flow from depth also exists. Baker and others (1989) have found evidence for two apparently independent fluid ejection events which, from their short duration and high implied flow rates, may have involved hydrofracture-enhanced permeability. Measurements by Bell (1989) suggest that pore pressures within an overpressured shale unit fall just below a critical level necessary to open fractures. This may also be the case in some Gulf Coast shales (Harrison and Summa, 1991).

The present study begins by presenting a simple model for oscillatory fluid release from a subsiding fluid pressure compartment. Different system behaviors, including unfractured steady states, oscillatory fluid release, and a steady fractured state are demonstrated topologically. A continuum dynamical model for subsidence, pressure generation and dissipation, and hydrofracturing is then presented. One-dimensional simulations of this model are presented which demonstrate the spatio-temporal development of some of the behaviors suggested by the topological analysis. Simulations show that tops of overpressured zones can under certain circumstances remain at a fixed elevation during sedimentary basin evolution (that is, act as a seal that propagates through the incoming rock column as a compaction/cementation/hydrofracture "front"). This suggests the possibility that fluid compartment seals undergo dynamic readjustment during basin evolution, as first suggested by Powley (1990).

## COUPLED HYDROLOGIC PHENOMENA: OVERPRESSURING, FRACTURING/HEALING AND FLOW

*A simple compartment model for episodic fluid release.*—Ghaith, Chen, and Ortoleva (1990) present a simple mathematical formulation for coupled fluid flow and fracture generation and healing based on conservation of fluid mass within a fluid compartment and an empirical permeability

dynamics (see also Chen and others, 1990). Figure 1 portrays the conceptual model, in which a large body of rock is hydraulically isolated from the surrounding basin by a relatively thin seal. Fluid release occurs through a puncture, or zone of hydrofracture, in the top seal bounding the fluid compartment. Let $p_c$ be fluid pressure within the compartment and $\kappa_s$ be the permeability within the putative puncture (assumed constant in space across the puncture). The dynamics of $p_c$ are obtained from fluid mass balance whereas that for $\kappa_s$ arises from fracture growth and healing/sealing processes.

The change with time of mols of water within the compartment of volume $V_c$ and porosity $\phi_c$ is given by

$$\frac{d}{dt}(\rho\phi_c V_c) = \rho\frac{d}{dt}(\phi_c V_c) + \phi_c V_c \frac{d}{dt}\rho \tag{1}$$

where $\rho$ is fluid molar density. The equation of state for water relates $\rho$ to temperature T and pressure p by

$$\rho = \bar{\rho}(1 + \beta(p - \bar{p}) - \alpha(T - \bar{T})) \tag{2}$$

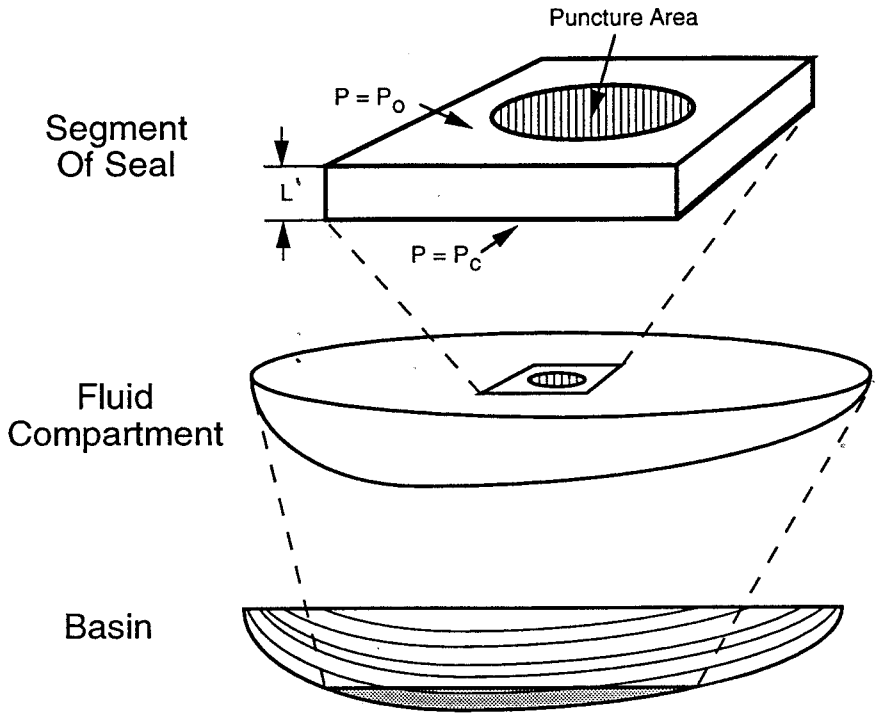


Fig. 1. Schematic portrayal of fluid compartment residing in a sedimentary basin, consisting of a large body of rock hydraulically isolated from its surrounding environment by seals. In this example the "bottom" seal consists of impermeable basement rock or sedimentary strata, while the top seal cross cuts strata.

valid for pressure and temperature deviations from a reference state (denoted by a superimposed bar) which are not too large. When considering loss of water by expulsion through a puncture in the compartment top boundary, or seal, the rate of change of mols of water within the compartment is equal to the rate of flow across the seal, expressed by

$$\frac{d}{dt}(\rho\phi_c V_c) = -\int_\Omega \rho\vec{q}\cdot d\vec{\Omega} \tag{3}$$

where $\vec{q}$ is the volume flux of water through the seal, and $d\vec{\Omega}$ is a surface element of the puncture area $\Omega$ times a unit normal pointing into the compartment (the integration is over the total puncture area $\Omega$). The seal containing the puncture in figure 1 is of thickness L and separates the compartment interior of fluid pressure $p_c$ from the surroundings, at pressure $p_o$. If porosity, permeability, and fluid density within the seal are constant, simple considerations of fluid mass balance yield the variation in pressure across the seal, in the z-direction (that is, vertical), to be

$$p = p_c + \frac{(p_o - p_c)}{L} z. \tag{4}$$

With the relation between pressure gradient and $\vec{q}$ as expressed in Darcy's law

$$\vec{q} = -\frac{\kappa}{\mu}\vec{\nabla}p \tag{5}$$

(here $\kappa$ is permeability, $\mu$ is fluid viscosity), the right-hand side of eq (3) equals $-\rho\kappa(p_o - p_c)A_c/\mu L$. Combining this with eqs (1), (2), and (3) and rearranging yields

$$\frac{dp_c}{dt} = \Lambda\kappa_s(p_o - p_c) + \tilde{\Gamma},$$

where

$$\Lambda = \frac{A_c}{V_c\phi_c\beta}$$

and

$$\tilde{\Gamma} = \frac{\alpha}{\beta}\frac{dT}{dt} - \frac{1}{\phi_c V_c \beta}\frac{d}{dt}(\phi_c V_c). \tag{6}$$

Here $\tilde{\Gamma}$ is a source term for fluid pressuring through compaction and thermal expansion, whereas the term including $\Lambda$ accounts for pressure dissipation by flow through the puncture. Eq (6) is similar to eq (13) in Domenico and Palciauskas (1988) but modified for the seal-puncture model given here.

One feature of this model necessary for development of oscillatory fluid release is the temporal dynamics of seal permeability $\kappa_s$. Fractures, if

interconnected, dramatically increase rock permeability. To account for this in the present model, it is assumed that the change in seal permeability with time is given by the following empirical law:

$$\frac{d\kappa_s}{dt} = g(\kappa_s, p_c). \tag{7}$$

The precise form of the source term g on the right hand side of eq (7) will depend on the precise kinetics of fracture growth and healing or sealing. What is important to consider here is that the fracture healing and/or sealing, and thus the associated loss in permeability, occurs in a time-dependent fashion. Hydrofracturing occurs when fluid pressure within a rock exceeds the least compressive stress plus the tensile strength of the rock. The critical pressure is denoted $p_f$. Similarly, fractures will close and eventually heal or become sealed when fluid pressure drops below some other critical value, denoted $p_h$. The jump in permeability accompanying hydrofracturing and the drop in $\kappa_s$ accompanying fracture healing or sealing are captured empirically by the form of the "null curve" $g(\kappa_s, p) = 0$ portrayed in figure 2.

Picture a scenario in which fluid pressure within the subsiding compartment is undergoing a slow increase with the seal in its unfractured state (lower branch in fig. 2). Once a critical fluid pressure is reached, fractures form, which dramatically increase permeability. The system experiences a jump from the lower to the upper branch of the $g = 0$ curve. The sudden increase in permeability leads to a greater rate of fluid expulsion through the seal. With subsequent fluid flow, pressure is lowered, and the state of the system moves along the upper branch, until the "healing pressure" $p_h$ is reached, whereupon fractures heal, and the system jumps back to the lower branch. Accompanying the fluid pressure/permeability hysteresis is an oscillatory flow of fluid released through the seal "puncture."

A qualitative analysis of the steady states of the model (eqs 6, 7) illustrates potential nonlinear dynamical behavior that can be obtained during fluid release from a fluid compartment. Steady (that is, time independent) states of the model are obtained by setting the right hand sides of eq (6) and (7) to zero:

$$g(\kappa_s, p) = 0 \tag{8}$$

and

$$\kappa_s = \frac{\tilde{\Gamma}}{\Lambda(p - p_o)}. \tag{9}$$

Distinct steady states of the system occur at the intersection of the null curves (eqs 8 and 9) and are schematically represented in figure 3. The positions of interesections are sensitive to many parameters, including the overpressuring rate and the magnitude of permeability enhancement

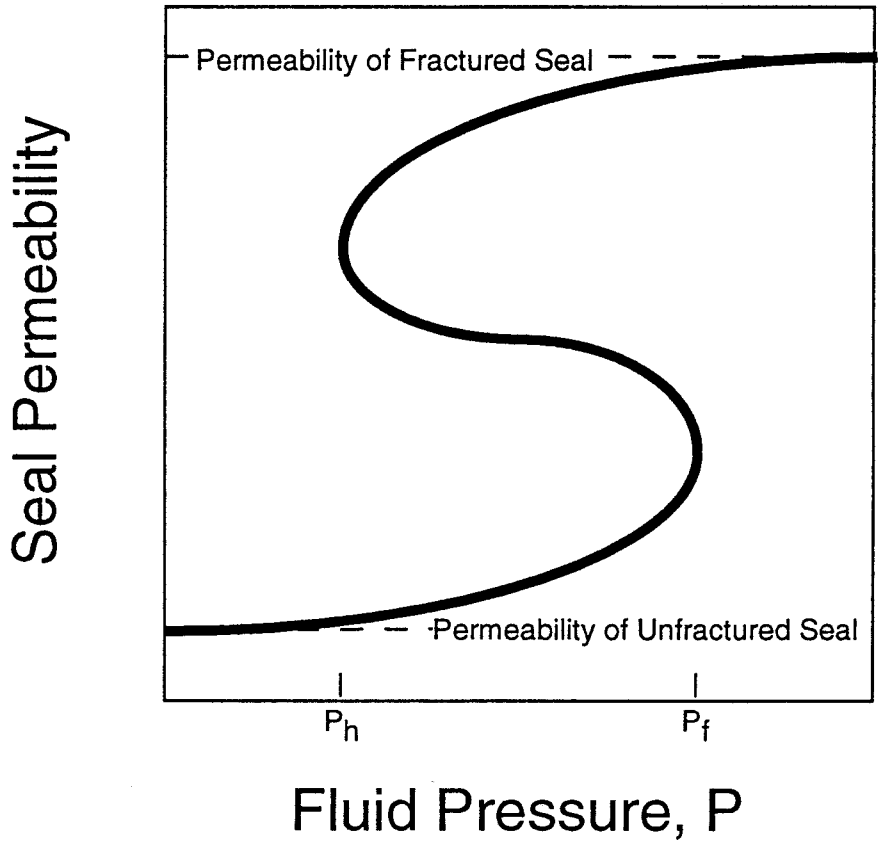


Fig. 2. Schematic dependence of seal permeability on fluid pressure. The "s" shape of this curve allows for a hysteresis and consequent cycling of permeability when the fracture dynamics underlying it is coupled to the relation for fluid mass balance. If fluid pressure in the seal exceeds a critical value, denoted $p_f$, and equal to the least compressive stress plus the tensile strength of the rock, the formation of natural hydrofractures causes the permeability to jump up to the upper branch of the "s" curve. Fluid pressure dissipation accompanying flow allows fractures to close and/or heal, whereupon the permeability regains the prefractured value. With further build-up of fluid overpressure, this scenario may continue in a cyclic manner (indicated by arrows), with the resultant episodic release of fluids from the compartment.

upon fracturing. In figure 3B seal permeability in the unfractured or healed state (lower branch of the $g = 0$ curve) is sufficiently large that the overpressuring rate is balanced by losses through the healed (or unfractured) seal. This is termed an "unfractured steady state." Figure 3C shows a "fractured steady state" in which the rate of fluid pressure increase is sufficiently large that the seal is held permanently "open" by hydrofractures. Figure 3D shows a case similar to 3B except that the indicated steady state exists close to the lower "knee." A system under

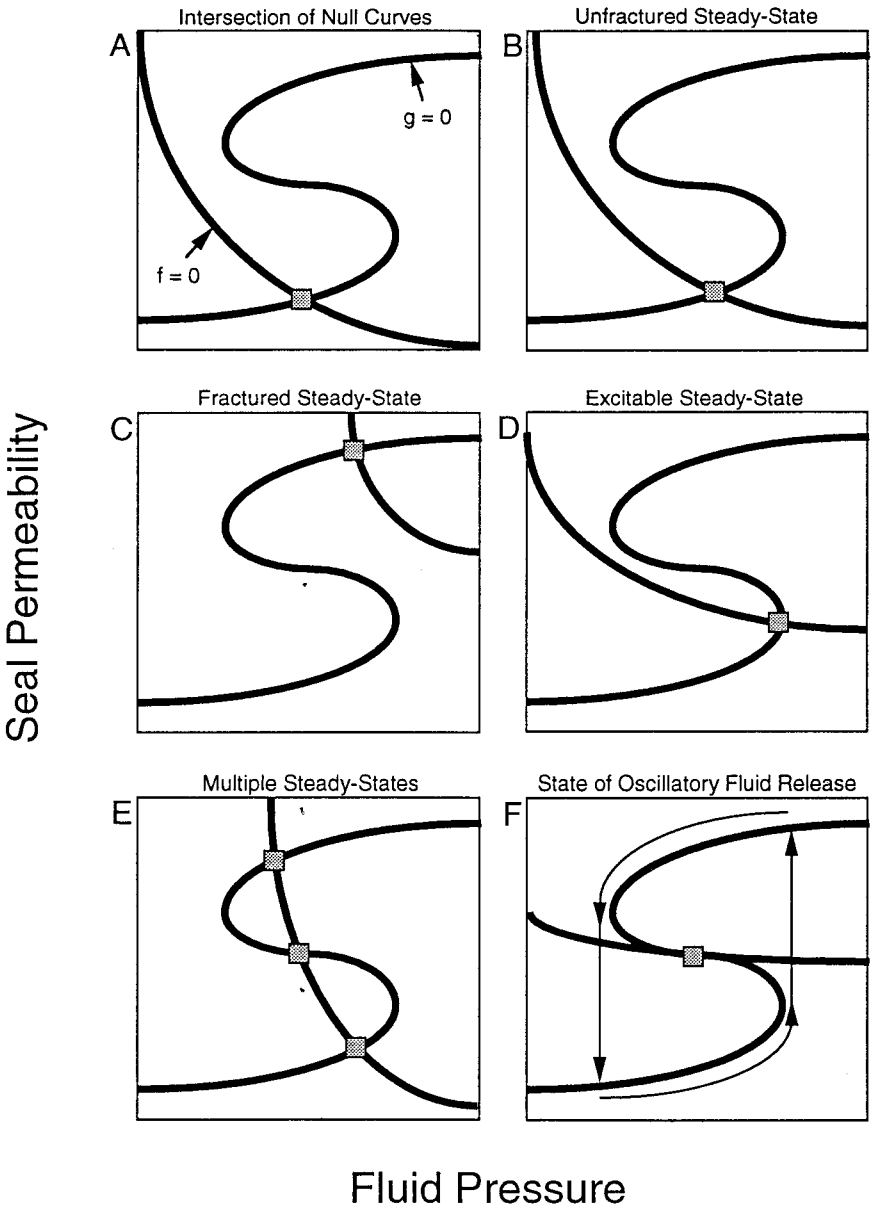


Fig. 3. Plots of the null curves of eqs (8) and (9) in the space of seal permeability and fluid pressure. (A) Intersections of the curves mark steady states achieved by the system (denoted by square-shaped markers). The position of steady states suggests the long-time behavior of the fluid compartment-top seal system. (B) Steady state resides on the lower, or unfractured, branch of the "s"-shaped curve. (C) Steady state resides on the upper, or fractured, branch of the "s"-shaped curve. (D) Steady state resides near the "knee" of the bottom branch and thus may be unstable to small, finite amplitude perturbations in fluid pressure. (E) Three distinct steady states here may be attained by the system. The actual state of the system will be history-dependent. The state on the middle branch is unstable to infinitesimal perturbations and, therefore is not obtained physically. (F) Unstable case, in which the steady state resides on the middle (unstable) branch. Here the system undergoes cyclic fracturing and healing with an accompanying oscillatory release of fluid from the compartment.

of pressure production on one side balance or exceed rates of pressure dissipation by flow across them.

The operation of any one of the scenarios suggested in the previous section is dependent on the cooperation of several processes, each with a characteristic time scale of operation. The relative rates of seal formation, pore pressure build-up, seal breaching (through natural hydrofracturing) and seal healing or sealing together become the deciding factors as to whether abnormally pressured fluid compartments form, where in the basin they reside, and how they persist through geologic time. The method presented here for analyzing how these processes interact involves casting the system dynamics in terms of coupled partial differential equations, which, as a direct reflection of the coupling, are non-linear. Simultaneous solution of these equations by numerical techniques simulates how the various processes influence one another by yielding the spatial and temporal changes in the system variables.

Validity of any system of differential equatons with respect to description of a natural process or set of processes depends on the completeness of the physics included in the mathematical description and the set of simplifying assumptions made. Domenico and Palciauskas (1988) discuss quantification of abnormal pressure generation due to several mechanisms and pressure dissipation from considerations of fluid mass conservation. Pressure-producing mechanisms discussed include loading due to sediment deposition and compaction, thermal expansion of aqueous fluid, and water-producing reactions through mineral phase transformations. A differential equation describing conservation of fluid mass in a small volume of compacting rock (derived below) contains terms accounting for the change in rock volume, fluid density, solid density, and flux of fluid out of the volume element (Palciauskas and Domenico, 1989).

To account for overpressuring, one need couple this equation with relations linking stress, fluid pressure, and temperature to changes in rock volume, fluid and solid density, and fluid flux (Palciauskas and Domenico, 1989). Because rocks are heterogeneous media, one need account for influences of rock texture on transmission and focusing of stress. Some account for a balance of forces as affected by gravitational body forces, and rock heterogeneity needs to be made. A distinction must be made between elastic deformation, which adiabatically follows other slower processes for most geological applications, and time-dependent mechanisms which lead to finite deformation; both influence the distribution of stress (Dewers and Ortoleva, 1990a). Because compaction in sedimentary basins can occur by mechano-chemical means (that is, intergranular pressure solution, Angevine and Turcotte, 1983; Walder and Nur, 1984; Houseknecht, 1988; Tada and Siever, 1989), the influence of pore fluid chemistry, solute transport, and water-rock reaction kinetics become other essential ingredients for a quantitative description (Dewers and Ortoleva, 1990a,b, 1993).

Quantification of deformation and water-rock interaction during diagenesis is complicated, involving elements of rock mechanics, reaction

kinetics, and mass transport. It is the coupling expressed in the non-linear terms of the differential equations, however, that is the critical element in understanding development of spatially localized or self-organized phenomena (Nicolis and Prigogine, 1977; Ortoleva and others, 1987, 1990; Ortoleva, 1993). In the present context, non-linearity is the essential ingredient allowing for the breaking of internal symmetry from an otherwise homogeneous or unpatterned state to a compartmented one in which domains of rock become hydraulically isolated from their surroundings (Dewers and Ortoleva, 1988).

## INTEGRATED REACTION-TRANSPORT-MECHANICAL MODELING

*Governing physical processes.*—The model described in detail below combines the chemical compaction dynamics set forth by Dewers and Ortoleva (1990a) with expressions for fluid mass conservation, Darcy flow, and rock dilatancy and permeability changes accompanying fracture formation and propagation. Specifically it describes interaction of the following processes:

A. poroelasticity of sediments undergoing burial;
B. water-rock reaction kinetics and solute transport;
C. chemical compaction due to pressure solution;
D. fracture propagation and healing; and
E. Darcy flow with grain geometry- and fracture-dependent permeability.

*Compaction model.*—A mathematical description of compaction involves processes cooperating on at least two length scales. Macroscopic processes described by continuum mechanics are strongly influenced by grain and smaller-scale processes, which in turn are affected by the macroscopic processes. In Dewers and Ortoleva (1990a), grain geometry is quantified in terms of truncated spheres in simple cubic packing. Porosity, grain number density, and contact areas of all grain facet types are found in terms of grain heights, widths, and radii of the truncated spheres. Decreases in grain height reflect compaction (by "pressure solution"), while increases in grain radius result from overgrowth. Overall rates of change of these variables are determined by the kinetics of pressure solution and overgrowth formation. Reactions involving, for example, aqueous silica are sensitive to the concentration of aqueous silica in the pore fluid. This in turn varies due to the mass transport mechanisms of advection and diffusion (we do not account for dispersion due to the low velocities of the flows of interest). Equations and variable definitions for this aspect of the model are summarized in table 1 and in the symbol table at the beginning of this paper.

*Poro-elasticity and macroscopic force balance.*—The macro-elastic formalism utilized by Dewers and Ortoleva (1990a) combines a constitutive relation between elastic effective stress and infinitesimal strain, which is fluid pressure dependent (Biot and Willis, 1957), with macroscopic force balance (accounting for gravitational body force) and the linear relation

TABLE 1.

*Chemical compaction and solute transport model*

*Evolution equations for grain geometry variables $L_z$, $L_y$, $L_x$, and $L_f$*

$$\frac{\partial L_i}{\partial t} = -\vec{u}\cdot\vec{\nabla}L_i + G_i \quad \text{where } i = f, x, y, z$$

*Conservation of solute mass at steady state*

$$-\vec{\nabla}\cdot\vec{J} = n\rho_s(A_z G_z + A_f G_f)$$

$$\vec{J} = -\phi D\vec{\nabla}c + \vec{v}\phi c$$

*Rate of strain for vertical compaction*

$$\frac{\partial u_z}{\partial z} = \frac{G_z}{L_z}, \frac{\partial u_y}{\partial y} = 0, \frac{\partial u_x}{\partial x} = 0$$

*Grain reaction rate laws*

$$G_z = \frac{2\pi D'\Delta}{A_z\rho_s}\{c - \tilde{c}(p, t)\exp[3(P_z - p)/\rho_s RT]\}$$

$$G_f = \frac{k^+}{\tilde{c}}\{c - c_f^{eq}\}, G_y = G_x = 0$$

between infinitesimal strain and elastic displacement. Macroscopic isotropy is assumed, with elastic constants that depend on porosity and degree of fracturing (Eshelby, 1957; Walsh, 1965; Zimmerman, Haraden, and Somerton, 1985). This part of the model is given in table 2; terms here are also defined in the symbol table.

*Fracture dynamics.*—For the present purposes, fractures are considered to be penny-shaped discontinuities in medium properties. Thermodynamic considerations indicate that fractures propagate if the crack extension force (Segall, 1984; also termed fracture propagation energy, Pollard and Aydin, 1988) exceeds a critical value. The former is proportional to the square of the stress intensity factor for dilational (that is, mode I) fractures, while the latter is related to the surface free energy of an ideal brittle solid (Segall, 1984; Atkinson, 1984). Fractures of finite length for which the crack extension force does not exceed the critical value are assumed to undergo healing (Segall, 1984). The rate of change of radius r of these fractures is taken to follow the law (Dutton, 1974, as given in Atkinson, 1984; see also Segall, 1984):

$$\text{rate of change of crack radius} = F = v_f\left[1 - \exp\left\{-\frac{U}{RT}\right\}\right]. \quad (10)$$

Here $v_f$ is a limiting propagation velocity that depends on the precise mechanism of crack generation. For sub-critical crack growth and healing, the rate limiting kinetic mechanism may be surface, grain-boundary,

TABLE 2.

*Poro-elastic model*

*Force balance*

$$\sum_{j=1}^{3} \frac{\partial \sigma_{ij}^{m}}{\partial x_i} - \{\phi\Gamma_f + (1 - \phi)\Gamma_s\}\delta_{iz} = 0, \qquad i = x, y, z$$

*Elastic effective stress-strain constitutive law*

$$\underline{\underline{\sigma}}^{m} + \alpha^{m} p \underline{\underline{I}} = \underline{\underline{\underline{\underline{C}}}}^{m} \underline{\underline{\epsilon}}^{m}$$

*Relation between compliance tensor and elastic moduli*
(from assumption of elastic isotropy)

$$C_{ijkl}^{m} = \mu^{m}\{\delta_{ik}\delta_{jl} + \delta_{il}\delta_{jk}\} + \lambda^{m}\delta_{ij}\delta_{kl}$$

*Relation between elastic strain and elastic displacements*

$$\epsilon_{ij} = \frac{1}{2}\left\{\frac{\partial w_i}{\partial x_j} + \frac{\partial w_j}{\partial x_i}\right\}$$

*Relation between intergranular stress and macroscopic stress*

$$-\sigma_{zz}^{m} = A_z P_z + (L_x L_y - A_z)p$$

or thin-film diffusion or reaction-kinetic controlled (Atkinson, 1984; Swanson, 1984; Smith and Evans, 1984). Eq (10) assumes fracturing is "reversible" and that fracturing and healing take place by the same mechanism. Factor U in eq (10) is (Segall, 1984; Atkinson, 1984) (see symbol table)

$$U = \frac{V}{a}\left\{\frac{\pi(1 - \nu^2)}{E} r\sigma_T^2 - Q\right\}. \tag{11}$$

The first term in eq (11) is the fracture propagation energy, while Q is the critical energy required for propagation. $\sigma_T$ in our model is equal to $p + \sigma_{xx}^{m}$, where p is fluid pressure, and $\sigma_{xx}^{m}$ is the horizontal component of the macroscopic stress tensor given in table 2 (and, by convention, is negative for compressive stresses). It is evident from this that, even if the tectonic environment for basins implies a compressive stress regime, a fluid pressure of sufficient magnitude may induce tensile stresses at textural flaws in rocks sufficent to initiate joint propagation (Pollard and Aydin, 1988). This critical fluid pressure, p*, is found from eq. (11) to be

$$p^* = \sigma_{xx}^{m} + \left(\frac{QE}{\pi(1 - \nu^2)r}\right)^{1/2}. \tag{12}$$

The latter term in (12) can be thought of as the tensile strength of the rock and decreases with increasing crack length.

As U in eq (11) is likely to be less than RT, we approximate eq (10) as follows (Segall, 1984):

$$F = \frac{v_f U}{RT}. \tag{13}$$

We wish to examine the consequences of placing this simple fracture dynamics into our continuum formalism for rock compaction and rock and fluid motion. To do so, we picture each macrovolume element to contain a number of typical fractures, each of half-length r and aperture a. The number density of fractures, or number of fractures per volume of rock when fracture volume is negligible, is denoted $\eta$. The quantification of a fracture network in this way, in terms of a series of parallel plates that are assumed to be interconnected, is commonly used in numerical modeling of flow in fractured rock (Wang, Tsang, and Sternbetz, 1983) and is deemed sufficiently rigorous for our purposes.The rate of change of length of a typical fracture within a macrovolume element of rock in the rock-fixed reference frame, allowing for rock flow, is

$$\frac{\partial r}{\partial t} = -\vec{u} \cdot \vec{\nabla} r + F. \tag{14}$$

The limiting propagation velocity, $v_f$, is taken to have the temperature and aperture dependence suggested by Smith and Evans (1984):

$$v_f = \frac{v'}{a^m T} \exp\{-E_f/RT\}. \tag{15}$$

Here $v'$, m, and $E_f$ (an activation energy) are dependent on the actual rate determining mechanism for fracturing. Data from Brantley and others (1990), assuming surface diffusion to be the rate-controlling mechanism, suggest

$$v' = 10^{-12} \text{cm}^6 \cdot {}^\circ\text{K/erg} \cdot \text{sec}$$

$$E_f = 8.0 \times 10^{11} \text{ erg/mol},$$

and

$$m = 2.$$

Q is taken to be $10^4$ erg/cm$^2$, suggested by Atkinson (1984) and Segall (1984). It is not clear that these results apply directly to natural hydrofractures. However, we have found that the actual time scale of fluid release is controlled by rates of fluid pressure dissipation. The kinetics of fracture generation given by the above mechanism is sufficiently fast such that it is not a rate-determining factor in fluid expulsion.

Fracture apertures are taken to have the functional dependence (Engelder and Scholz, 1981; Walsh and Brace, 1984)

$$a = \bar{a} + b \ln \left[ \frac{P_{eff}}{\bar{P}} \right] \tag{16}$$

where $P_{eff}$ equals $-\sigma^m_{xx} - p$, $\bar{P}$ is a reference pressure, $\bar{a}$ is the aperture at the reference pressure, and b is a parameter characterizing the asperity height distribution within fractures. This shows that as $P_{eff}$ (implicitly positive definite) increases, fracture apertures decrease logarithmically.

Values for $\bar{a}$, b, and $\bar{P}$ are suggested from data on artificial joints in sandstones by Engelder and Scholz (1981). Increase in fracture aperture can be self-limiting because of the increased stress it causes in the direction normal to the fracture plane. For simplicity here, we impose a truncation of the aperture so that if $-\sigma^m_{xx} < p$, apertures do not widen without bound but obtain a maximum value taken here to be 10 microns. Thus with truncation understood, the relation in eq (16) is always defined. Initial crack radii are taken to be one tenth of the grain size, as suggested by Atkinson (1984).

Examination of the form of eqs (10) and (11) shows that as fracture length increases, the tensile stress necessary to propagate fractures decreases with the inverse square root of fracture length; this suggests an unstable situation in which fractures grow without bound for constant stress conditions. However, a number of natural limitations on propagation of fractures arise, particularly in the case of hydrofractures. Mechanical interaction between propagating crack tips can limit fracture propagation, such that as a fracture network develops, average fracture length is related to average fracture spacing (Pollard and Aydin, 1988). While quantification of such effects are beyond the scope of this paper, we nonetheless constrain the growth of fractures in order to reflect this type of mechanical interaction by setting an upper bound on fracture length to be the inverse cube root of fracture density.

Porosity and permeability increase accompanying fracture dilation (Domenico and Palciauskas, 1988) can prevent the unbounded growth of fractures. As hydrofractures grow, the additional pore volume generated leads to dissipation of fluid pressure (Rice and Rudnicki, 1979; Etheridge, Wall, and Vernon, 1983), so that fractures may grow only long enough to create sufficient volume such that the critical condition for hydrofracturing is no longer satisfied. Also, enhanced permeability created by fractures can limit fracture growth by a fluid flow-related dissipation of fluid pressure. In this regard, hydrofracture growth and resultant pore fluid release may be self-limiting.

*Fluid pressure generation and dissipation.*—Fluid flow, the generation and dissipation of abnormal fluid pressures, and the coupling between

fracture generation and fracture permeability enter the model by an expression for water conservation:

$$\frac{\partial \rho\phi}{\partial t} = -\vec{\nabla} \cdot (\vec{v}\rho\phi) \tag{17}$$

where $\rho$ is fluid molar density, and $\vec{v}$ is fluid velocity. With Darcy's law we have (Palciauskas and Domenico, 1989)

$$\phi(\vec{v} - \vec{u}) = -\frac{\kappa}{\mu}\vec{\nabla}\psi \tag{18}$$

where $\vec{v} - \vec{u}$ is fluid velocity relative to the rock matrix (the latter moving at deformation velocity $\vec{u}$), $\kappa$ is permeability, and $\mu$ is the fluid viscosity. $\psi$ (the pieziometric fluid pressure) is defined by

$$\psi = p + \Delta g z \tag{19}$$

where $\Delta$ is the fluid mass density, g is the acceleration due to gravity, and z is position along the vertical direction. The right hand side of eq (18) is the volume flux of fluid $\vec{q}$ as used earlier in eq (5), but we allow for rock flow as well in eq (18).

Flux of fluid through a volume of fractured rock occurs both through the fracture network and porous matrix. It is commonly assumed that both are described by Darcy flow but with a different functional dependence of permeability on pore and fracture shape and size (Freeze and Cherry, 1979). If we assume hydraulic equilibrium between the system of pores and the system of fractures, the volume flux of fluid equals the sum of contributions from both pores and fractures. With this eqs (17) and (18) combine to yield

$$\frac{\partial \phi\rho}{\partial t} = \vec{\nabla} \cdot \left(\left(\frac{\kappa^*}{\mu}\right)\rho\vec{\nabla}\psi\right) - \vec{\nabla} \cdot (\vec{u}\rho\phi) \tag{20}$$

where $\kappa^*$ is the total permeability,

$$\kappa^* = \kappa_m + \kappa_f. \tag{21}$$

The subscripts m and f refer to matix and fracture, respectively; expressions for $\kappa_m$ and $\kappa_f$ adopted here are explicitly defined below. Note that in eq (20) $\kappa^*$ should be a tensor to reflect preferred directions of flow due to fracture orientation; as the actual simulations to be carried out here are in one dimension, we do not develop this point further here. For two and three dimensions, a tensorial permeability should be considered.

The equation of state for the fluid is taken in the form presented earlier in eq (2). We will assume that $\alpha$, $\beta$, and $\mu$ are constant; furthermore, temperature is taken to depend only on depth, being determined by a fixed geothermal gradient. We will denote the z-components of rock and fluid flow velocity as u and v, respectively.

Combining eqs (2) and (20) yields for variation only along the vertical (z) direction

$$\phi \frac{\bar{\rho}}{\rho} \beta \frac{\partial \psi}{\partial t} + \frac{\partial \phi}{\partial t} = - \frac{\partial}{\partial z}(u\phi) + \frac{\partial}{\partial z}\left(\frac{\kappa^*}{\mu} \frac{\partial \psi}{\partial z}\right) - \left\{u - \frac{\kappa^*}{\phi\mu} \frac{\partial \psi}{\partial z}\right\} \cdot \left\{\phi \frac{\bar{\rho}}{\rho}\left(\beta \frac{\partial \psi}{\partial z} - \alpha \frac{\partial T}{\partial z}\right)\right\}. \quad (22)$$

The ratio $\beta(\partial\psi/\partial z)$ divided by $\alpha(\partial T/\partial z)$ is much less than one for common fluid pressure and temperature gradients in the crust; hence the influence exerted by the $\beta(\partial\psi/\partial z)$ term on the right hand side of eq (22) is negligible. Similar arguments lead one to conclude that the $\bar{\rho}/\rho$ term may be considered unity. With this, eq (22) becomes

$$\phi\beta \frac{\partial \psi}{\partial t} + \frac{\partial \phi}{\partial t} = - \frac{\partial}{\partial z}(u\phi) + \frac{\partial}{\partial z}\left(\frac{\kappa^*}{\mu} \frac{\partial \psi}{\partial z}\right) + \left\{u - \frac{\kappa^*}{\phi\mu} \frac{\partial \psi}{\partial z}\right\} \phi\alpha \frac{\partial T}{\partial z}. \quad (23)$$

Eq (23) couples fluid pressure generation due to compaction and fluid thermal expansivity with fluid pressure dissipation by fluid flow and rock dilatancy from fracturing. It is an expanded version of the relation presented in app. A of Palciauskas and Domenico (1989), although we neglect the elastic compressibility and thermal expansion of the porous matrix as they influence pore pressure. This is because the irreversible deformation of porous media exerts a far greater influence on fluids over geologic time than does the infinitesimal deformation associated with elastic strain (Palciauskas and Domenico, 1989), and the expansivity of water is at least an order of magnitude greater than that of the solid matrix that contains it (Bradley, 1975; Domenico and Palciauskas, 1988).

Noting that $\eta$ is defined as the number of fractures per volume of the rock when the fracture volume ($\pi r^2 a$) is negligible, the total porosity is found in terms of the porosity of the array of spheres in simple cubic packing, $\phi_w$ (the 'w' refers to the work of Weyl, 1959, who was first to quantify compaction in terms of this grain geometry) and the fracture parameters $\eta$, r, and a by

$$\phi = 1 - \frac{(1 - \phi_w)}{(1 + \eta\pi r^2 a)}. \quad (24)$$

The relationship between grain geometrical parameters and $\phi_w$ is found in Dewers and Ortoleva (1990a). The matrix porosity is found from

$$\phi_m = \frac{\phi_w}{(1 + \eta\pi r^2 a)} \quad (25)$$

and fracture porosity from

$$\phi_f = \frac{\eta\pi r^2 a}{(1 + \eta\pi r^2 a)}. \tag{26}$$

Note that $\phi_m + \phi_f = \phi$.

A number of formulas exist for the dependence of permeability on both fracture and grain textural parameters. Matrix permeability is commonly modeled from either the Kozeny-Carman relation (Scheidegger, 1974; Ungerer and others, 1990), the Hagen-Poiseville equation (Scheidegger, 1974) or a porosity power law (Angevine and Turcotte, 1983; Walder and Nur, 1984; Barcilon and Richter, 1986). We will discuss the influence of porosity on matrix permeability below. The permeability of a fracture described as two parallel, flat walls with mean separation a is equal to $a^2/12$ (Engelder and Scholz, 1981; Walsh and Brace, 1984; Brown, 1989). The permeability of a volume element containing a network of fractures is taken to be the permeability of a single fracture multiplied by the fracture porosity (Freeze and Cherry, 1979). These formulas are summarized in table 3 in terms of the variables used here. Here we examine a simple dependence of matrix permeability on porosity although expressions allowing for a more specific dependence on grain geometrical variables may be derived.

TABLE 3.

*Permeability formulas and miscellaneous data*

*Matrix permeability*

Kozeny-Carman relation

$$\kappa_m = \frac{\phi_w^3}{5S_o^2(1 - \phi)}$$

$S_o$ = surface area of solid/unit volume of solid
$= n A_f/(1 - \phi)$

Porosity power law for permeability

$$\kappa_m = \kappa'\phi_w^n,\ \kappa' = 10^{-8}\ \text{cm}^2$$

$$5 < n < 8$$

*Fracture permeability*

"cubic" law

$$\kappa_f = \phi_f \frac{a^2}{12}$$

$\mu = 10^{-2}$ Poise
$\beta$ = 3.3 E-11 dyn/cm$^2$
$\Delta$ = 1 g/cm$^3$

$\Gamma$ = 9.8 E2 g/cm$^2$/s
$\Gamma_s$ = 2.45 E3 g/cm$^2$/s
$\alpha$ = 1.0 E-3 °C$^{-1}$

*Numerical simulation of the model.*—Numerical simulations of the model as given in tables 1 and 2, with eqs (13), (14), and (23) were carried out to delineate phenomena supported by our model. The system was subject to burial, subsidence, and typical basin stresses. The study is restricted to one spatial dimension—all variables depend only on the vertical (z) dimension. The physical situation is as suggested in figure 4; simulation domains were envisioned as being of infinite horizontal extent, with no horizontal gradients in any of the descriptive variables. The system extends from the Earth's surface to a subsiding impermeable basement rock or impermeable sedimentary strata. Figure 4, B and C, schematically represents the overall scenario for fluid compartment dynamics from a simple one-dimensional perspective. The solution domain encompasses the rock in between the transect Z-Z′ in figure 4A. With burial, the length of the transect increases, compaction progresses, overpressures may develop, and possibly hydrofracturing occurs. A seal may be defined as the zone in which fluid pressure gradients depart appreciably from the hydrostatic gradient and corresponds to a permeability minimum. This is shown in figure 4, B and C.

Burial is simulated by specifying the injection rate and character of sediment entering the top boundary ($z = 0$) of the basin. Fluid pressure is maintained at 1 bar at the top boundary, and a no-flux condition ($\partial\psi/\partial z = 0$) is imposed at the sediment-basement interface. Temperature follows a linear gradient (30°C/km); we assume a constant surface temperature of 15°C. Letting $u_o(t)$ be the rate (m/yr) of deposition, then $u(z, t)$, the z-component of the rock flow velocity, satisfies

$$u(0, t) = u_o(t) \tag{27}$$

for specified $u_o(t)$. Furthermore, the texture of the material deposited (that is, at the top of the simulation domain) must be specified:

$$L_z(0, t) = L_z^*(t) \tag{28}$$

and similarly for the other grain dimension variables. The sediment is taken to be in the interval

$$0 < z < Z(t).$$

The depth $(-Z)$ of the "basement sediment interface" is determined from $u(z, t)$ via

$$\frac{dZ}{dt} = u(z, t). \tag{29}$$

This must be solved simultaneously with the pressure solution, compaction equation for the truncated sphere model:

$$\frac{\partial u}{\partial z} = G_z/L_z. \tag{30}$$

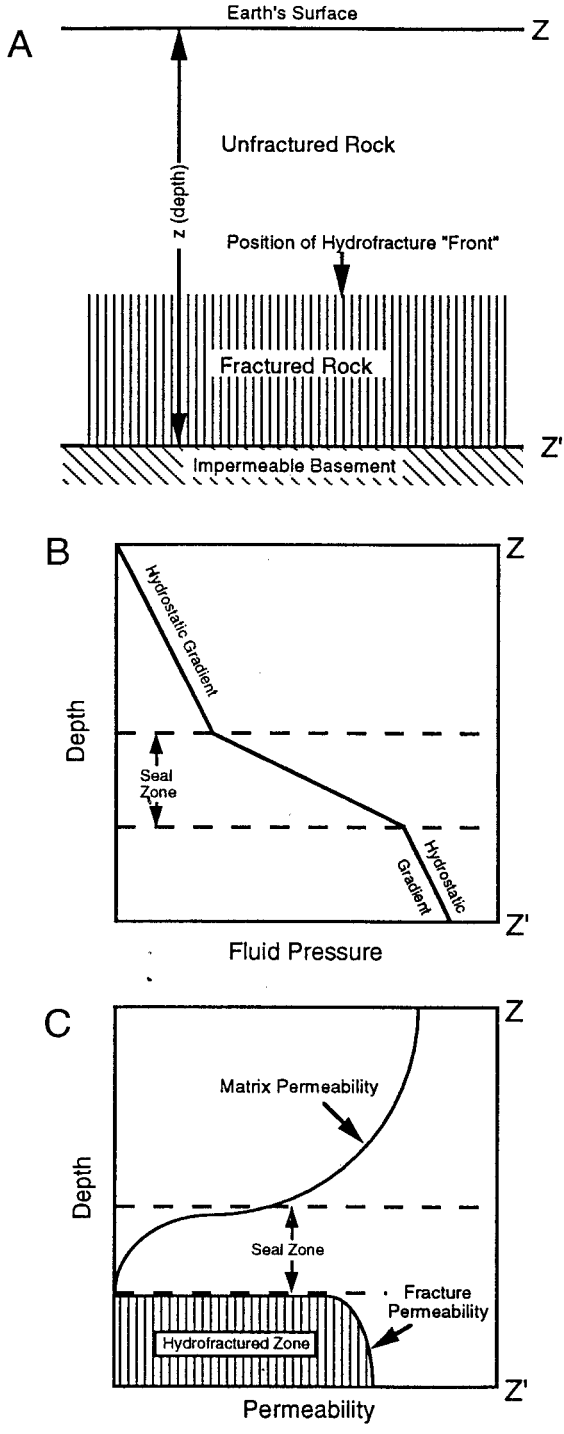
A
Earth's Surface
Z
Unfractured Rock
z (depth)
Position of Hydrofracture "Front"
Fractured Rock
Z'
Impermeable Basement
B
Z
Hydrostatic Gradient
Depth
Seal Zone
Hydrostatic Gradient
Z'
Fluid Pressure
C
Z
Matrix Permeability
Depth
Seal Zone
Fracture Permeability
Hydrofractured Zone
Z'
Permeability

For numerical computations it is convenient to introduce a normalized depth $\xi$ defined as

$$\xi = z/Z(t). \tag{31}$$

The bottom of the simulation domain is thus at $\xi = 1$; all equations are solved on this fixed domain ($0 < \xi < 1$). This is a convenient method for numerical solution, as no modification of the spatial discretization grid associated with $\xi$ need occur during a run. This transformation does, however, introduce the complexity that as the height of the sediment pile increases, numerical resolution worsens as distance with respect to z between adjacent grid points increases.

Further details of the calculations are as follows. Integrating eq (30) from 0 to Z(t) and using eqs (29, 31) we obtain

$$\frac{dZ}{dt} = u_o + Z \int_0^1 d\xi G_z/L_z \tag{32}$$

where all variables are now considered to be functions of $\xi$ and t (rather than z and t). Note that $dZ/dt$ and $u_o$ are both negative, reflecting the fact that the "basement"-sediment interface descends as sediment is deposited (downward) upon the sediment pile; however, the second term on the right hand side of eq (32) is positive—that is, compaction ($G_z < 0$) insures that $dz/dt$ must be less than $u_o$ in absolute value. Eq (32) is solved numerically using a trapezoidal approximation for the $\xi$-integral. To complete the description we specify no-flux boundary conditions for solutes at both boundaries, and at the bottom for $\psi$. $\psi$ equals 0 at the top boundary.

As a result of the change of variables ($z \rightarrow \xi$), the form of the equations involving a time derivative is modified. For example, the first

Fig. 4. Representation of a simulation domain modelling a basin subject to sedimentary loading and basement rock subsidence, showing relationships between fluid pressure, "seal" position, permeability, and fracture density. (A) Simulation domain is a one dimensional traverse Z (surface of Earth) to Z′ (impermeable basement). It is assumed that there are no horizontal spatial gradients in any of the system variables. Also depicted here is the position of a hydrofracture "front," which is shown to arise in some of the simulations of later figures. Sediment of a constant initial texture is added at the top boundary, and the bottom boundary subsides at a given velocity. (B) A schematic plot of fluid pressure as a function of distance along the traverse Z-Z′ (depth) in a typical simulation. In the upper position of the domain, the pores are sufficiently connected that the fluid is maintained at hydrostatic pressure. Beneath the seal is a zone of natural hydrofracturing induced by the fluid overpressure. Because the excess permeability of rock containing the fractures allows for relatively rapid hydraulic communication throughout the fracture domain, the fluid pressure gradient again achieves a hydrostatic value, but the fluid pressure here is greater than hydrostatic, illustrating overpressure. (C) Fracture density and whole rock permeability as a function of distance along the traverse Z-Z′. The permeability decreases initially with depth due to loss of pore space by compaction but increases dramatically within the zone of hydrofracturing. The "seal" corresponds to a permeability minimum and may be quite broad (hundreds of meters).

equation in table 1, for $L_z$, becomes

$$\frac{\partial L_z}{\partial t} = -\frac{1}{Z}\left(u - \xi \frac{dZ}{dt}\right)\frac{dL_z}{d\xi} + G_z \tag{33}$$

and similarly for $L_x$, $L_y$, and $L_f$. The essence of the simulation technique is then to transform all equations to the $\xi$, t variables and solve them on a regular grid in the interval $0 < \xi < 1$. The textural equations are integrated using a simple forward time difference method, the $\partial/\partial\xi$ terms being "upwinded." The transformed elliptic equations (for pore fluid concentrations, pieziometric pressure, and elastic displacements) are solved using ELLPACK (Rice and Boisvert, 1985).

Boundary conditions for elastic displacements are set as follows. Vertical gradients of the three components of elastic displacement at the top boundary are kept at a level consistent with 1 bar hydrostatic pressure. The z-component at the bottom of the domain is set at an arbitrary reference value. Lateral stresses are found in terms of vertical (lithostatic) stress multiplied by a constant, which we took to vary between .3 (roughly that for zero lateral strain) and 1 (wherein horizontal stresses equal the lithostatic stress). Constraint of the lateral stresses gives us additional degrees of freedom such that we may reduce the number of equations for elastic displacements to that for the vertical (z) component.

Compaction rates are determined by a water-film diffusion mechanism, although sandstones may undergo pressure solution by other mechanisms as well (Tada and others, 1987). In our model compactional porosity loss is an important source for generation of fluid overpressures, and so our results are highly dependent on compaction rates and thus on the actual pressure solution mechanism. While we have found fundamental differences in behavior between pressure solution mechanisms with respect to, for example, formation of stylolites (Dewers and Ortoleva, 1990a), the main conclusions of this paper are unaffected by the choice of one pressure solution mechanism over another. A further discussion of this aspect of the model is found in Dewers and Ortoleva (1990a).

The compaction model utilized in this paper differs from that of Angevine and Turcotte (1983): we account for solute mass transport, influences of textural heterogeneity on effective stress; we do not assume that pore fluid concentration is determined by equilibria between fluid and quartz-free faces, and we examine the case of uniaxial, not isotropic, compaction. Furthermore, we account explicitly for the fluid pressure dependence of compactional rates, and the compaction model is solved simultaneously with the equation for the fluid pressure (eq 13). Nevertheless, our porosity-depth profiles for simulations with negligible overpressure are similar to those obtained by Angevine and Turcotte (1983), which were shown by them to be similar to those observed in quartz arenites by Schmidt and McDonald (1979). Also, in accord with their results, little pressure solution occurs at depths shallower than 1 km. To maximize production of fluid overpressure by compaction, we have run

our simulations using very-fine grain size. Because of the grain size dependence of the compaction law, this has the effect of lowering porosity faster at a given depth than for coarser grain sandstones. Our choice of a fine grain sandstone is in a sense an average over a range of grain sizes from shales to coarse grain sandstones. Further details on the specific assumptions used in our compaction and permeability models are summarized in tables 1 to 3.

## SIMULATION OF TOP SEAL FORMATION AND OSCILLATORY FLUID RELEASE

Our simulations based on numerical solution of the model equations demonstrate widely varying behaviors with changes in sediment burial, compaction, overpressuring, and hydrofracturing. In the following sections we discuss examples that we feel emphasize some of the more important features and point out the diversity of behaviors obtained. In so doing we demonstrate a degree of universality between formation and maintenance of abnormally pressured fluid compartments and other non-linear dynamical phenomena. Our study is by no means exhaustive, and much work remains.

*Effects of burial rate variations.*—The Ghaith and others (1990) model described in an earlier section demonstrates a transition between steady unfractured, oscillatory or steady fractured states (compare fig. 3B, C, and F). A shift in the curve labeled "f = 0" relative to that labeled "g = 0" produces the change in behavior. Even though it is not clear that results from that model, which has no spatial dependence, can be straightforwardly applied to the present one, we expect that the change in parameters corresponding to this shift in curves should in the present model yield a similar transition. In particular, from the form of eqs (8) and (9), an increase in $\bar{\Gamma}$, a parameter in eq (9) which increases proportionally with burial rate, produces a change from unfractured to oscillatory behaviors.

In figure 5, we show the progressive burial and compaction experienced by a column of constant inlet texture and initial sediment pile height of 1.5 km, undergoing progressive burial and compaction. Frame (A) shows the time evolution of the fluid pressure at the bottom of the simulation domain, while frames (B) through (E) show spatial variations in the variables. Profiles of (B) piezometric fluid pressure $\psi$, (C) porosity $\phi$, (D) $L_z$ (grain height), and (E) $L_f$ (grain radius) are illustrated as a function of depth for simulation times of 0 (broken line), 25 (dotted line), and 50 (solid line) million years (Ma).

Figure 5A shows the (total) fluid pressure at the bottom of the simulation domain as a function of time after 5 Ma of burial. Prior to this point, the shortening of the rock column due to compaction was faster than the rate of thickening due to sedimentation at the top. At approx 18.5 Ma, overpressure begins to build, and the rate of change of pressure steepens. At about 23 Ma, the pressure-time profile attains a slope similar to that at the earlier stages of the simulation. Because we have used a constant burial rate (modified somewhat by compaction), we

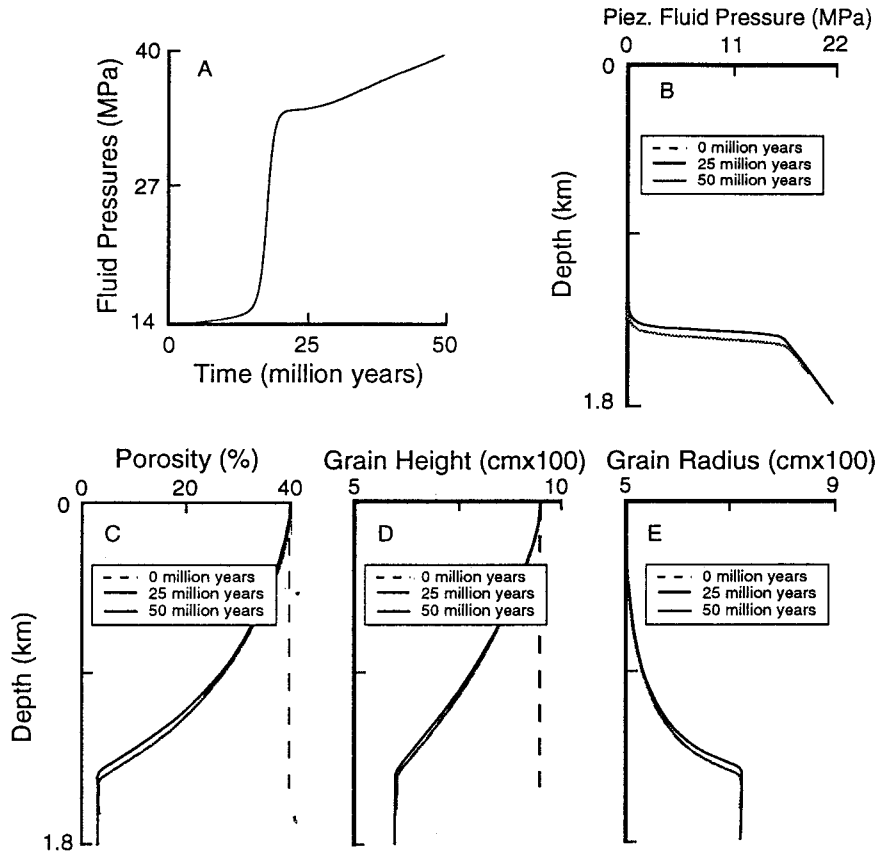


Fig. 5. Simulation of burial and compaction of a sediment pile consisting of very-fine grains modeled as truncated spheres in simple rectangular packing with a sedimentation rate of 15.8 m/Ma. (A) Plot of fluid pressure at the bottom of the simulation domain as a function of simulation time (we plot data only after 5 Ma; prior to this time the rate of domain length shortening due to compaction exceeds the rate of domain length increase due to sedimentation). Changes in the profile with time between 5 and 14 Ma reflect a hydrostatic pressure with depth, while the rapid rise between 14 and 23 Ma records the development of overpressure due to compaction and thermal expansion of the fluid. The change in pressure with time after 23 Ma shows a slight decrease in rate of overpressure-generation, but the pressure gradient at the bottom of the simulation domain remains larger than the hydrostatic gradient. (B) Pieziometric fluid pressure as a function of distance along the simulation domain at 25 Ma (dotted line) and 50 Ma (solid line). Negligible pieziometric pressure develops at depths less than 1.1 km. Between 1.2 and 1.4 km, however, a rapid rise is evident, corresponding to the rise seen in (A). At depths greater than ~ 1.4 km, the pieziometric pressure continues to increase linearly with depth. Profiles with depth of porosity (C), grain height ($L_z$, D), and grain radius ($L_f$, E). The porosity decreases monotonically until the depth where significant overpressure develops, after which all compactional porosity loss ceases. The grain textural parameters responsible for the changes in porosity reveal some interesting structure. Grain height decreases with depth, reflecting shortening of grains due to pressure solution. Grain radius increases with depth, reflecting overgrowth formation. Changes in $L_f$ and $L_z$ can be attributed largely to local exchange of mass between grain contacts and grain free faces, that is, all quartz dissolved at contacts is gained by local precipitation at free faces. However, there is a small amount of quartz cement that can be attributed to advective mass transport from deeper to shallower depths, evident in the small maximum in $L_f$ at about 1.3 km. The lesser amounts of cement at deeper depths are balanced by a slightly greater amount of grain shortening, with the overall effect of maintaining a relatively constant porosity. This simulation is an example of an "unfractured steady state" shown in figure 3B.

can roughly interchange time and depth. The profile in figure 5A thus appears very similar to pressure-depth profiles above and inside overpressured fluid compartments (see examples in Bradley, 1975; Powley, 1980, 1990; Tigert and Al-Shaieb, 1990; and Hunt, 1990). The transition zone, or region of higher-than-hydrostatic pressure gradient, occurs between 1.3 and 1.4 km.

The burial rate for the run is 15.8 m/Ma and is sufficiently slow that, as compaction proceeds and overpressure develops, the leakage of fluids through the rock column maintains a balance with the rate of pressure generation; the level of overpressuring is sufficient to slow compaction to an almost vanishing rate, as is evident from the $L_z$ profile, but does not induce hydrofracturing. With time, solutes carried by the flow from greater depths begin to cement the rock at approx 1.4 km. This produces a small maximum in the $L_f$ profile and a porosity minimum at the final simulation time, but the effect is not a large one.

Differences in position between the middle and final times in, for example, figure 5B show that little change in the position of the inflection point in the porosity profile (at about 1.4 km) has occurred between 37 and 50 Ma.

Figure 6 shows a simulation run at a higher sedimentation rate, 88.4 m/Ma. Here the behavior is much the same, but the rise in pieziometric pressure is sufficiently great by about 13 Ma to induce hydrofracturing in the rock at about 2.3 km. The change in fluid pressure at the bottom of the simulation domain with time is shown in figure 6A. Spatial profiles at simulation times of 0, 10, and 15 Ma are shown for pieziometric fluid pressure (fig. 6B), porosity (fig. 6C), and fracture radius (fig. 6D). The position of the inflection point in the final porosity profile is at a greater depth than in figure 5, otherwise profiles of framework grain texture variables for this run look very similar to that in figure 5. The pieziometric fluid pressure builds to a maximum, whereupon it is seen in figure 6C to level off to a constant (pieziometric pressure profiles at the initial and middle simulation times coincide with the bottom axis). This leveling off is due to hydrofracturing; the resultingly greater fracture permeability allows hydraulic communication within the fractured zone and thus dissipation of any pressure gradients that deviate from the hydrostatic. Figure 6D shows fracture lengths greater than the initial fracture size in this zone and reveals some internal structure with respect to the distribution of fracture lengths reflecting the interplay of fracture growth, fracture healing, and fluid released by hydrofracturing. Figure 6A appears very similar to figure 5E, until approx 13.5 Ma, the point at which hydrofractures develop, whereupon the fluid pressure is seen to undergo one relatively large oscillation, followed by several very small oscillations. The first oscillation is due to fluid pressure decrease accompanying the increase in fracture porosity and fluid release, while the latter small amplitude fluctuations in fluid pressure are an artifact of the numerical resolution. Each of the small waveforms beginning at approx 14 Ma correspond to the development of fractures at one spatial point. The

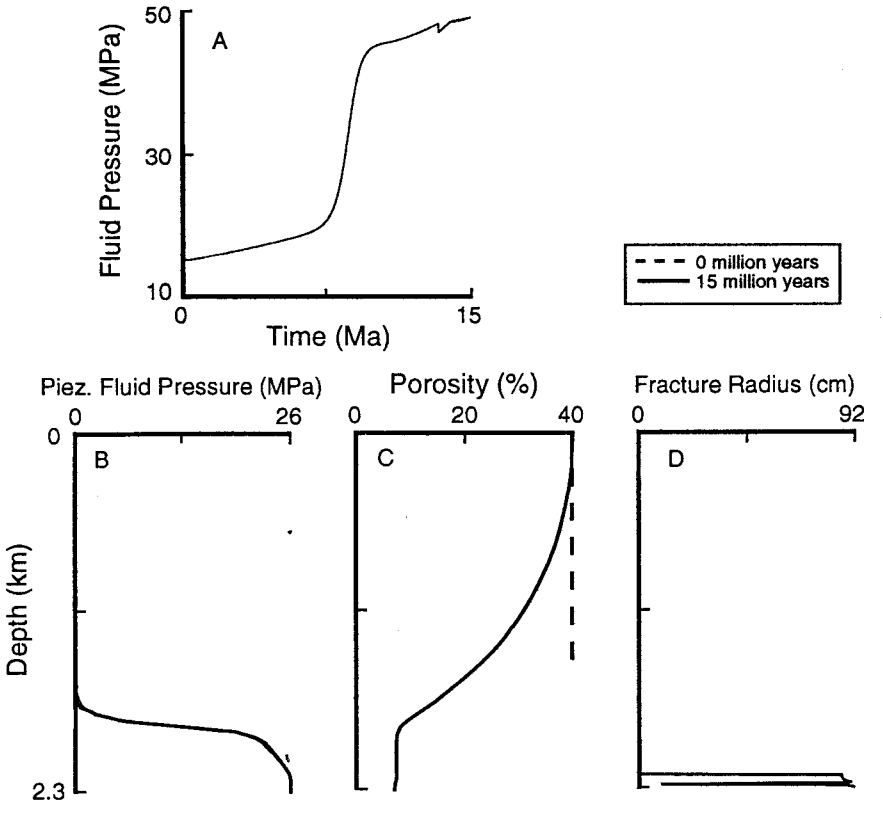


Fig. 6. Similar to figure 5, except that the sedimentation rate here is 88.4 m/Ma. The burial rate of the rock column is sufficiently fast that large overpressures build up. As a result, hydrofracturing occurs when the fluid pressure exceeds the critical value given by eq (12). The changes in fluid pressure at the bottom of the domain are very similar to those of figure 5A, until approx 13 Ma when fractures develop. Here the pressure drops suddenly, then builds up to a level characterized by an approximately linear change with time (the small fluctuations at the end of the simulation, between about 14 to 15 Ma, are an artifact of the numerical resolution). (B) Changes in the pieziometric pressure with depth are similar to those seen in figure 5 until the time of hydrofracturing. This constant value in space at 2.2 to 2.3 km is a reflection of dissipation by flow of any gradient in pieziometric pressure due to the enhanced hydraulic conductivity of fractured rock. (C) Changes in porosity with depth show a slowing of compaction rate due to overpressure development, but the loss of overpressure due to fracturing allows compactional porosity loss to commence at the bottom of the simulation domain. (D) Fracture radius profile with depth at 15 Ma, showing the zone of hydrofracturing. The spatial profiles of variables are shown at 0 Ma (dashed line), 10 Ma (dotted line), and 15 Ma (solid line). This simulation demonstrates the achievement of a "fractured steady state" suggested in figure 3C.

height and amplitude of these "numerical" fluctuations decrease with increasing numbers of grid points; however, the long computer times associated with finer grid spacing make these studies impractical for the algorithms utilized in the present work. The variations reflect, we feel, a

steady fractured state in which rates of fracturing and healing are balanced by rates of fluid pressure dissipation and correspond to the state portrayed in figure 3C. This state was proposed by Walder and Nur (1984; they term this a "quasi-equilibrium"). Thus, with a slight increase in subsidence rate, system behavior shifts from a steady unfractured state, that depicted in figure 5, to the steady fractured case shown in figure 6.

With further increase in subsidence and sedimentation rate, we find that a transient phase of oscillatory fluid release accompanying hydrofracture formation precedes the onset of a steady fractured state. This is shown in figure 7 for a subsidence rate of 158 m/Ma. A and B of figure 7 show fluid pressure at the bottom of the simulation domain and position of the minimum permeability across the simulation domain, as they vary with time. In a manner different to the cases of figures 5 and 6, the fluid pressure in figure 7A rises until approx 6.6 Ma, whereupon hydrofractures develop. The fluid pressure then is seen to undergo a series of oscillations of progressively decreasing amplitude until they are damped out. Figure 7B shows that the minimum permeability in the sediment column, which for this run corresponds to the permeability just above the zone of hydrofracturing, rises to a certain level and then remains at a relatively fixed depth (in this case, about 2.2 km). This corresponds to a dynamically varying zone of hydrofracturing, which maintains a fixed position with respect to the top of the sediment column. In the frame of reference moving with the rock, this would appear as a front of hydrofracturing which sweeps through the rock column. We believe that the observation by Bell (1989) in Gulf Coast shales, stating that only small variations in fluid pressure would be required to open fractures, is indicative of a steady fractured state as obtained here by numerical solution of the model.

A and B of figure 7 suggest a particular sequence of events in which a domain of a rock column undergoing burial and compaction at sufficient rates has initial overpressure development, a hydrofracturing event, a period of episodic fluid release, and finally a steady state of fracturing and fluid pressure production/dissipation in which the upper boundary of the zone of hydrofracturing remains at a fixed depth. C and D of figure 7 allow closer examination of the fluid pressure oscillations and the position of the shallowest depth of hydrofracturing seen in figure 7A and B. From a comparison of these two curves, we see that the episodic fluid release reflected in large amplitude fluid pressure oscillations accompanies a sinking zone of hydrofracturing, while small amplitude variations beginning at about 8.2 Ma and representing a steady state of fracture production and fluid leakage coincide with a relatively static upper position of the hydrofracturing zone.

To provide an explanation for the change in behavior, we again look to the topological analysis of the Ghaith, Chen, and Ortoleva (1990) model. Upon hydrofracturing (at around 6.6 Ma in fig. 7A) a period of oscillatory fluid release occurs for approx 2.6 Ma, whereupon the system then settles into a steady fractured state (limited again by the numerical

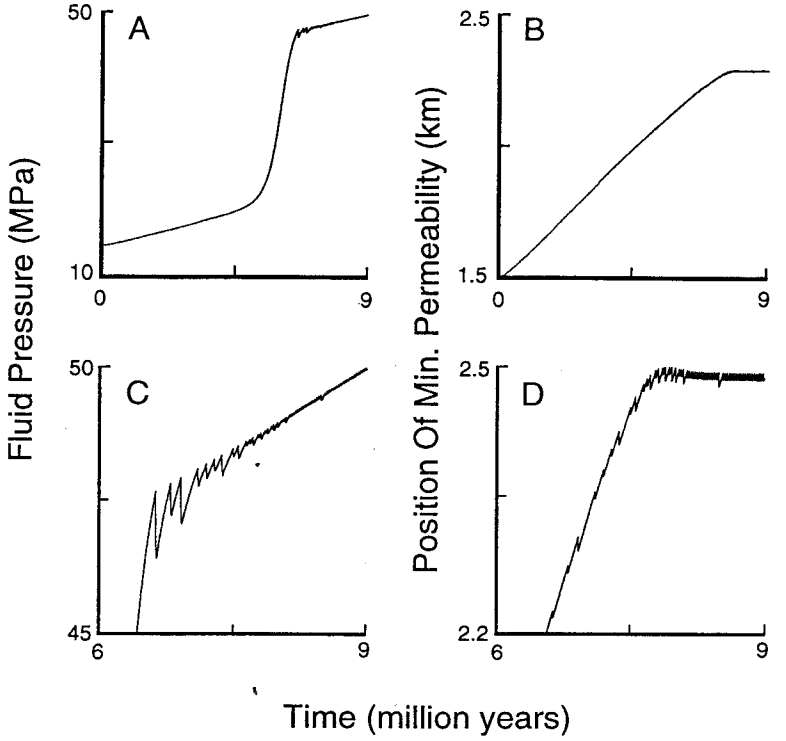
A
B
C
D
50
10
0
9
2.5
1.5
45
6
2.2
Fluid Pressure (MPa)
Position Of Min. Permeability (km)
Time (million years)

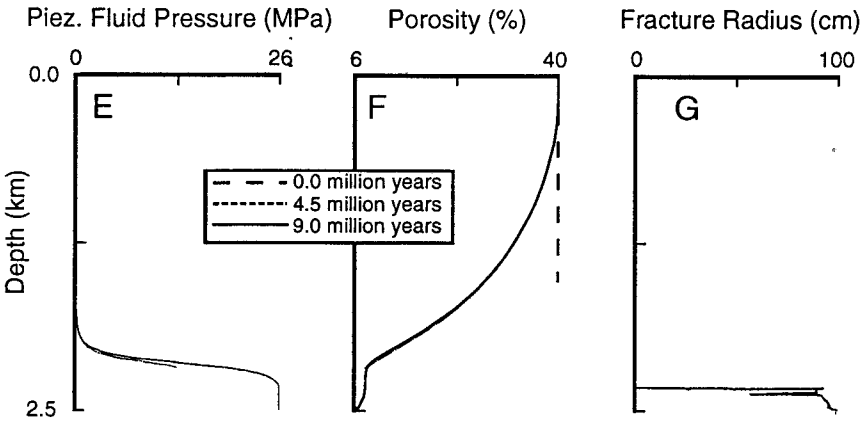
Piez. Fluid Pressure (MPa)
Porosity (%)
Fracture Radius (cm)
E
F
G
0.0
26
6
40
100
2.5
Depth (km)
0.0 million years
4.5 million years
9.0 million years

resolution).The oscillatory state corresponds to figure 3F, while the steady fractured state is graphically portrayed in figure 3C. An upward shift in the curve plotting the relation in eq (4), corresponding to the steady-state of the fluid mass balance relation (eq 2), would take the system from the behavior of figure 3F, oscillatory fluid release, to that of figure 3C, the fractured steady state. From the form of eq (4), we see that a decrease in parameter $\Lambda$ could produce this shift. $\Lambda$ is proportional to the ratio between the fracture "puncture" area and the compartment volume in the Ghaith, Chen, and Ortoleva (1990) model and, in the present one-dimensional study, would be analogous to the inverse of the height of the "fluid compartment," that is, the distance from the bottom of the simulation domain to the top of the hydrofractured zone. Because the height of the hydrofractured zone increases with time in our simulation (analogous to a decrease in $\Lambda$), the behavior of the coupled flow/fracture system changes from one of oscillatory fluid release to one of steady fracture propagation/fluid pressure dissipation with increasing geologic age.

One difference between the oscillatory fluid release obtained in our model and that suggested in the treatment of Ghaith and others (1991) and Chen and others (1990) is that total healing of fractures is not a necessary element of the present dynamic. The fracturing/healing cycle of the study of Ghaith, Chen, and Ortoleva (1991) and Chen and others (1990) can be replaced by the imposition of unfractured rock due to burial into a spatial domain in which the stress conditions are, or become, favorable for fracturing.

---

Fig. 7. Similar to figures 5 and 6 except that the rate of sedimentation is increased to 150 m/Ma. (A) Change with time of fluid pressure at the bottom of the simulation domain. The profile reflects a hydrostatic gradient existing at the domain bottom between 0 and 5.4 Ma and between 7 and 9 Ma and a greater than hydrostatic-fluid pressure gradient between 5.4 and 7 Ma. After an initial build-up of overpressure, the fluid pressure undergoes a brief transient period of oscillation, corresponding to episodic release of fluids to the above sediment due to the initiation of fractures and then settles down to an approximately steady, linear increase with further time. (B) Change in time of the depth at which the permeability is a minimum. The depth initially increases, reflecting the greater porosity loss at the domain bottom. At greater depths where hydrofracturing occurs, the rate of increase of the position of the permeability minimum slows until it attains a steady, constant position with time. This corresponds to the steady-fractured case suggested in figures 3C and 6 and shows that such a state is characterized by a steady fracture front (just beneath the permeability minimum) with respect to the subsiding rock-fixed reference frame. Frames (C) and (D) show in detail the large fluid pressure variations attending the transient oscillatory phase and the smaller variations (due to numerical resolution) of the steady fractured states. The unphysical fluctuations of position of the permeability minimum correspond to fracturing developing at a single spatial grid point in the numerical discretization. (E) Porosity profiles with depth for simulation times of 0 Ma (dashed line), 6 Ma (dotted line), and 9 Ma (solid line). A slight plateau in porosity with depth is still evident but is less prominent than the cases seen in figures 5 and 6. (F) Piezometric pressure with depth, showing the transition zone (or seal) and the plateau that would yield a fluid pressure versus depth profile similar to that depicted in figure 4B. Note that while the piezometric fluid pressure is constant in space at depths deeper than $\sim$2.1 km, it is not necessarily constant in time as shown in frame (A). (G) Profile of hydrofracture radius with depth at simulation time of 9 Ma.

*Influence of textural dependence of matrix permeability.*—In the previous simulations, we have used a porosity power-law for the matrix permeability with an exponent of 8, as suggested by Angevine and Turcotte (1983). Barcilon and Richter (1986) found that segregation of melt from solid matrix occurred as this exponent passes through a critical value, showing that this is an important non-linearity in their model. We expect similar behavior to arise in the present model. To test this, in figures 8 and 9, we show results for power-law exponents of 5 (fig. 8) and for the Kozeny-Carman relationship, in which permeability is proportional to the porosity raised to the third power. These simulations were run at a burial rate of 158 m/Ma, the same as the case presented in figure 7.

In figure 8A, we see that the transition in fluid pressure is more discontinuous than for the higher exponent case of figure 7. Also, as can be seen in the blow-up of figure 8A presented in figure 8B, fluid pressure at the bottom of the simulation domain undergoes a few large amplitude fluctuations and then quickly settles down to a steady state of fracturing/fluid release (the small fluctuations occurring after about 7.4 Ma again are an effect of the spatial discretization). The character of the waveform and its change in time are markedly different from that seen in figure 7, A and C. Obviously, the exact functional dependence of permeability on porosity exerts a strong influence on the possibility for and the nature of fluid release from compartments.

This point is underscored by the simulation run with the Kozeny-Carman relationship shown in figure 9. We see that no overpressuring

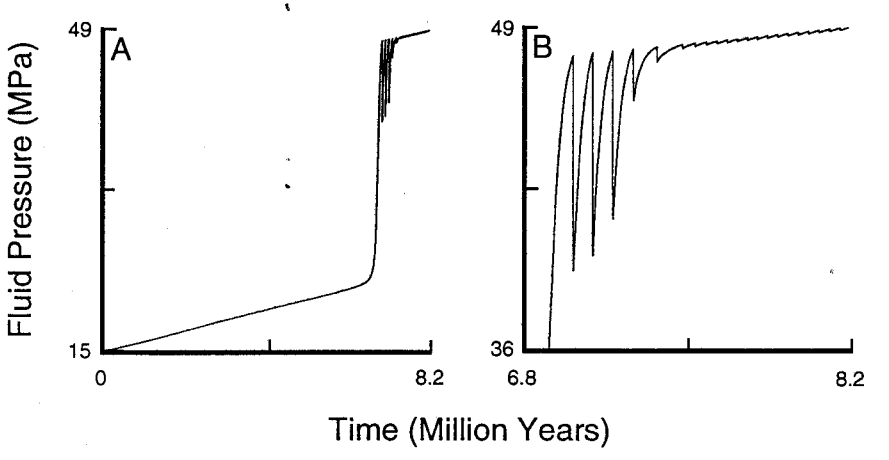


Fig. 8. Similar to figure 7 except that the permeability varies as $\phi^5$. We plot the fluid pressure at the bottom of the simulation domain as a function of time in the first frame and show more detail after 6.8 Ma in the second frame. While the qualitative behavior of the system is the same as in figure 7, that is, a transient period of large amplitude fluid pressure oscillations followed by a steady-state of fracture production and fluid release, the quantitative behavior is strikingly different. The coupled dynamics of fluid flow and hydrofracturing are sensitive to the exact textural dependence of the permeability.

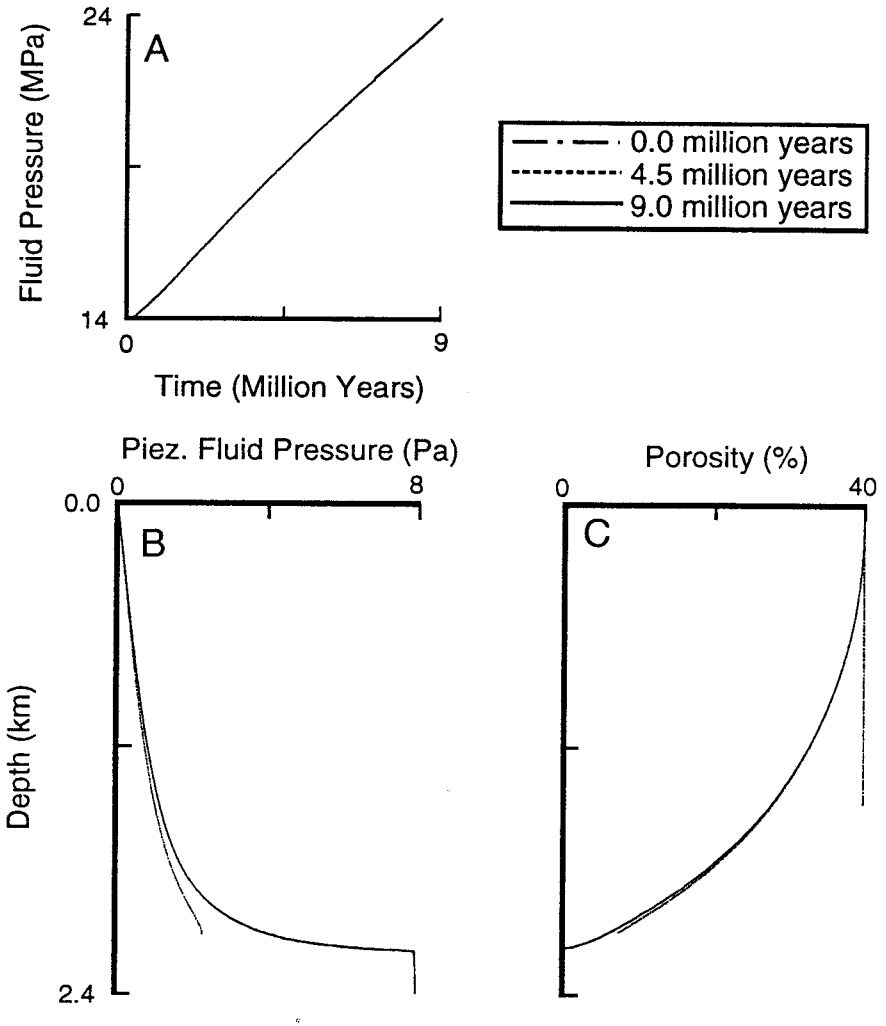


Fig. 9. Same as figures 7 and 8, except that we use the Kozeny-Carman relation between porosity and permeability. Negligible overpressures develop because the larger permeabilities allow for rapid dissipation of overpressuring. Porosity decreases with depth in this case, with no inflection evident.

develops; the slight curvature in the fluid pressure-time profile of figure 9A is due to compactional shortening of the simulation domain. A negligible amount of pieziometric pressure development is seen to occur at the final time of 9 Ma in figure 9B. The porosity decreases steadily with depth (for numerical reasons the porosity does not vanish, but rather we allow it to decrease to a constant value of 0.01 percent). The inflection is

seen in figures 5C, 6C, and 7E and occurs because overpressuring slows compaction; the overpressuring and hence the inflection in the porosity are not found here.

We conclude that if a porosity-permeability power law relationship is valid, then an exponent of at least 5 is necessary to develop sufficient overpressures to induce hydrofracturing for the parameters used to generate figures 7, 8, and 9. This critical value is expected to change with input sediment texture, subsidence rate, thermal gradient, and probably other factors as well. More generally, we expect that the overpressuring and the onset of hydrofracturing require a sufficiently strong dependence of permeability on porosity and other textural variables.

*Influence of lateral basin stresses.*—Magnitudes of horizontal stresses in sedimentary basins range from about 0.3 to 1.0 of the vertical or lithostatic stress (McGarr, 1988; Palciauskas and Domenico, 1989). We expect that as the least compressive horizontal stress enters into the criterion for hydrofracturing, in eq (12), the magnitude of horizontal stresses applied at the side boundaries of the basin will be an important factor in the formation of fluid compartments and oscillatory fluid release. To test this, we show in figures 10 through 13 the effects of increasing the ratio of the magnitude of the horizontal to vertical stress from 0.33 (fig. 10), to 0.40 (fig. 11), 0.45 (fig. 12), and lastly 0.5 (fig. 13). All these simulations were performed with a burial rate of 500 m/Ma, which is large but below the upper bound on natural sedimentation and subsidence rates.

In figure 10, we see the fluid pressure at the bottom of the simulation domain as a function of time (fig. 10A) and the pieziometric fluid pressure, porosity, and fracture radius as functions of depth for the simulation times of 0, 2.6, and 4 Ma (fig. 10B-D). Large amplitude oscillations in the fluid pressure occur upon hydrofracturing between 2.8 and 4.0 Ma. The pieziometric fluid pressure rises to a constant value at about 2.6 km, indicating a hydrostatic pressure gradient from 2.6 km to the bottom of the simulation domain. Porosity decreases steadily with depth, but a small inflection is evident at about 2.5 km, corresponding to the top of the overpressured zone. This zone is also one of hydrofracturing, seen in figure 10D. Small amplitude fluctuations in fracture radii with depth are evident. The latter can be correlated with the pressure fluctuations of frame A. There are 15 oscillations in frame A and 13 oscillations in frame D. Thus present day fracture-depth data may contain information on oscillatory fluid release.

Figure 11 shows a simulation with the same parameters as in figure 10, except that the ratio of horizontal to vertical stress is increased to 0.4. Fluid pressure oscillations at the sediment-basement interface are shown in figure 11A. If we count the smaller amplitude couplets together as one large oscillation, then the number of oscillations in figure 11A is the same as in figure 10A. However, the average amplitude of the oscillations in figure 10A is roughly 80 bars, while that in figure 11A is roughly 40 bars. The maximum pressure achieved by the system represented by figure 11

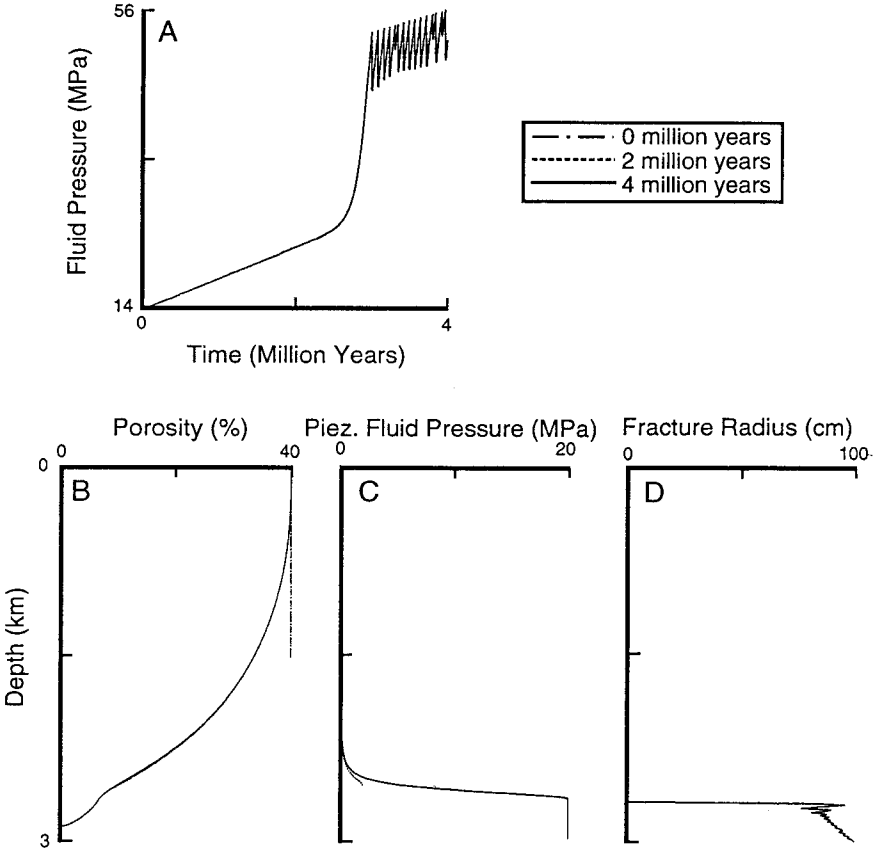


Fig. 10. Simulation of burial and compaction in a sediment column subject to lateral stresses that are approximately one-third of the lithostatic stress. The sedimentation rate in this case equals 500 m/Ma. (A) Plot of fluid pressure at the bottom of the simulation domain as a function of time. Upon hydrofracturing, large amplitude oscillations in fluid pressure are evident. The two styles of oscillation may suggest the existence of an underlying multiple state structure analogous to that of figure 3E or chaotic oscillation. (B) Porosity versus depth. (C) Pieziometric fluid pressure with depth. (D) Fracture radius with depth. The profiles at 0 Ma (dashed line), 2.6 Ma (dotted line), and 4.0 Ma (solid line) are shown.

is about 40 bars greater than that represented by figure 10. The pieziometric fluid pressure within the "compartment" oscillates about a higher average value here than in the case of figure 10; it attains a value almost 50 bars greater at the final time of 4.0 Ma, shown in figure 11B. The higher amount of overpressure in this case has impeded compaction to a greater degree, as can be seen in the larger inflection of the porosity profile in figure 11C at about 2.5 km. The average amplitude of the

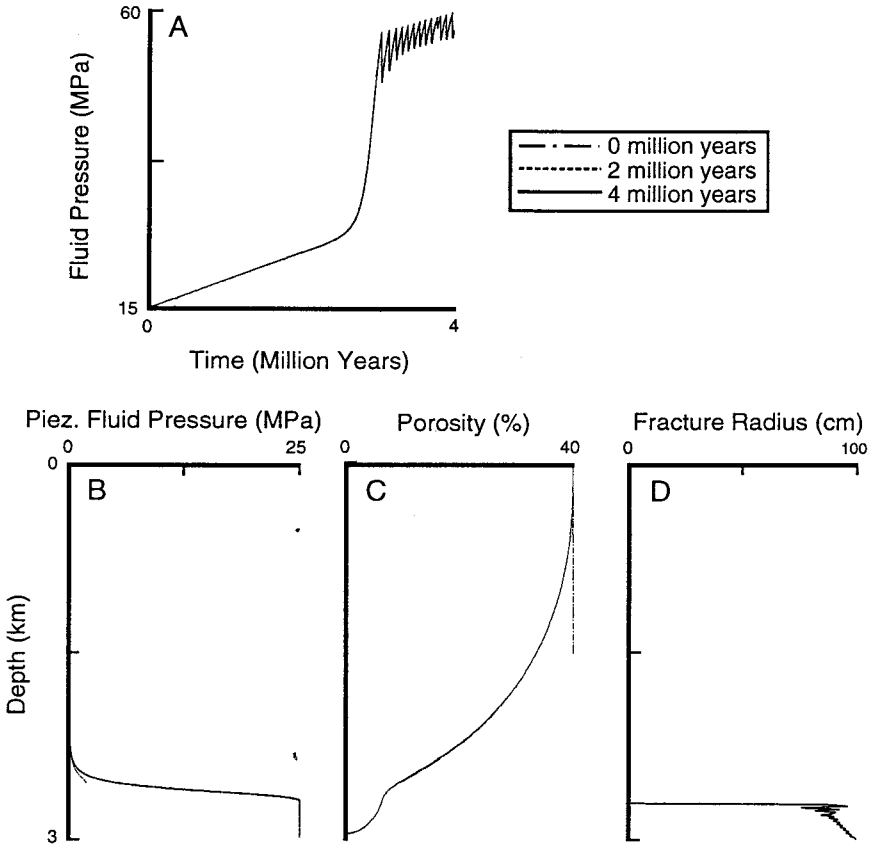


Fig. 11. Same as figure 10 except that the ratio of horizontal to vertical stress here is 0.4. (A) Fluid pressure of the domain bottom as a function of time. The oscillations in this case look similar to those in figure 10, except the amplitude is smaller, and the peak pressure of each oscillation is greater in value. (B) Profile of pieziometric fluid pressure with depth. This value around which the pieziometric fluid pressure within the hydrofracture zone varies is greater than in figure 10. (C) Profile of porosity as a function of depth. The inflection in the curve is more pronounced than in figure 10. (D) Profile of hydrofracture radius as a function of depth.

fluctuations in the fracture radii in figure 11D is slightly greater than that in figure 10D.

With only a small increase in the ratio of horizontal to vertical stress to 0.45, a markedly different behavior is achieved; this is shown in figure 12. Again hydrofracturing accompanied by oscillatory fluid release occurs when overpressure develops to a critical level, but here, in figure 12A, the period of oscillation initially is twice that, but then settles into a period equal to the periods of the previous two simulations of figures 10 and 11. The amplitude of oscillation here is also much less, although the

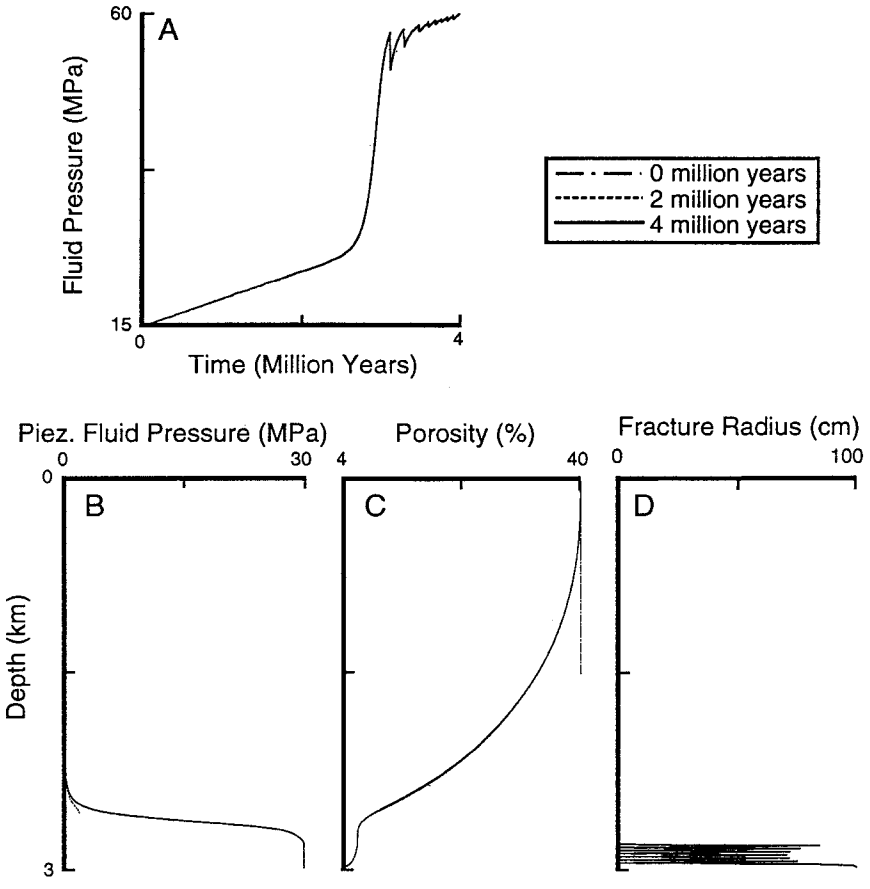


Fig. 12. Same as figures 10 and 11 except here the ratio of horizontal to vertical stress is 0.45. (A) Fluid pressure at the bottom of the simulation domain as a function of time. Upon hydrofracturing, a transient period of oscillation occurs followed by a steady-fractured type of behavior, similar to that seen in figures 7 and 8. (B) Profile for pieziometric pressure versus depth. (C) Porosity versus depth. Compactional porosity loss has almost stopped for a small interval in depth. (D) Fracture radius versus depth. The large amplitude fluctuations of fracture radius record the cyclic fracture growth and healing.

maximum fluid pressure achieved during the simulation is about 20 bars greater than that in figure 11A. The spatial profile of pieziometric pressure is similar to the other two cases, but the transition to the plateau, or leveling off of the pressure due to fracture-enhanced hydraulic conductivity, is seen to be smoother in figure 12C than in figures 10C or 11C. Porosity attains a slight plateau with depth, reflecting a greater influence of fluid pressure on compactional rates. The most dramatic difference in the results of this run from the previous two are seen in the spatial

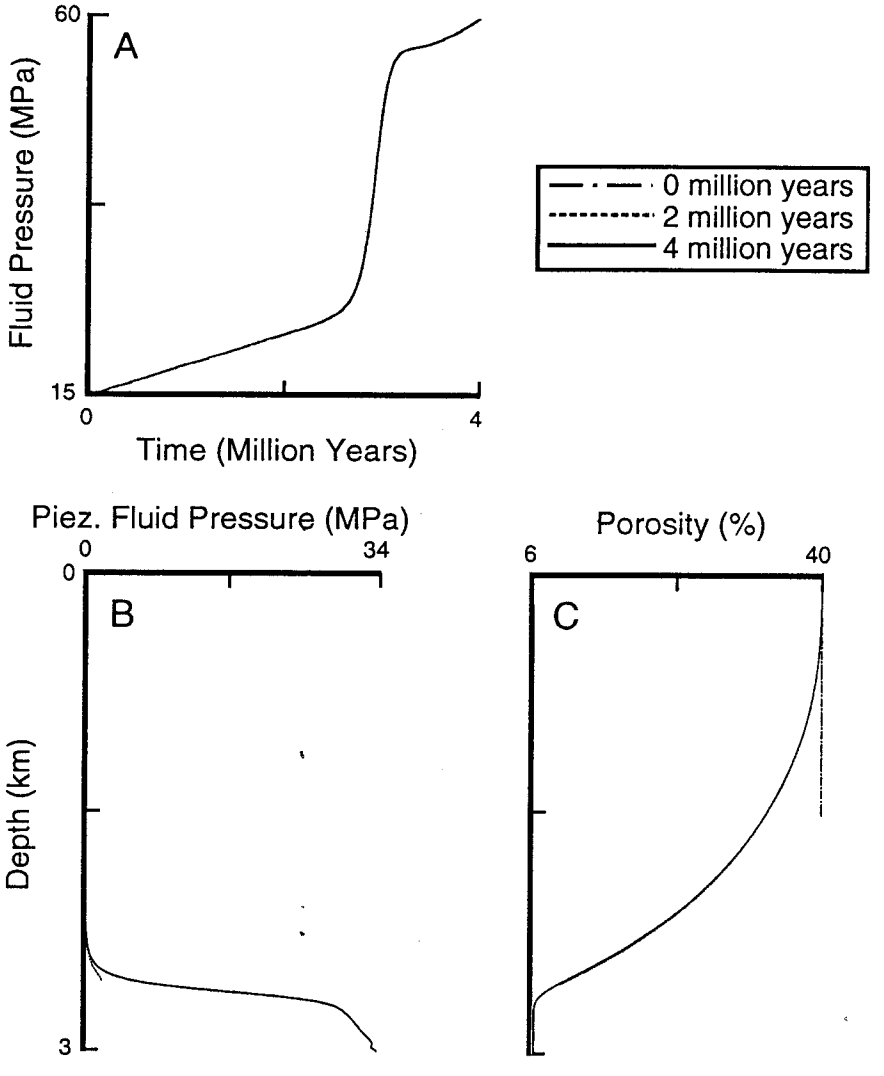


Fig. 13. Same as figures 10, 11, and 12, except here the ratio of horizontal to vertical stress is 0.5 and is sufficiently large to prevent the formation of hydrofractures, unlike the previous three figures. (A) Fluid pressure at the domain bottom as a function of time. Note the similarity between this and figure 5A. (B) Profile of porosity with depth. Compactional loss of porosity has almost ceased at depths greater than 2.4 km.

profiles of the fracture radii in figure 12D. From this it is evident that a cyclic propagation and healing of fractures have taken place. Each of the fracture maxima corresponds to one of the maxima in the time course of fluid pressure (frame A) except that the most deeply buried fracture,

maximum correlates with the first two fluid pressure oscillations. The distance between adjacent fracture maxima in figure 12D (about 22 m) divided by the subsidence rate (500 m/Ma) (about 44,000 yrs) is close to the period of the pressure oscillations in figure 12A (approximately 75,000 yrs). The differences can be attributed to compactional shortening of the rock columns. This is the only simulation we show that exhibits complete healing of fractures.

Finally, in figure 12, we show consequences of increasing the stress ratio to 0.5. Here, at least for the period of this simulation, the increased horizontal stress coupled with loss of fluid pressure through the rock column is sufficient to retain the level of rise of overpressure beneath that necessary for hydrofracturing. Compactional loss of porosity has almost ceased at about 2.6 km (although some small variation is evident). The pieziometric fluid pressure increases monotonically; a small fluctuation at about 2.9 km coincides with the porosity variation at this depth.

The previous four cases demonstrate a transition from oscillatory fluid release accompanied by minimal healing of fractures to oscillatory release accompanied by cyclic fracture growth and healing to the unfractured steady state, all with only small variations in lateral stress. This suggests that the tectonic setting of a basin will strongly influence the manner in which the interplay between rock compaction, fluid expulsion, and hydrofracturing may proceed.

## CONCLUDING DISCUSSION

We have presented a coupled model of fluid flow, compaction, and hydrofracturing in porous media. The quantitative predictions of our model depend strongly on the compaction mechanism, the relationship between rock texture and permeability, and other lithologic characteristics.

A viable model for the formation of dynamical seals bounding a compartment from the top must account for the following:

- –a mechanism for porosity and permeability loss through time-dependent compaction and/or cementation;
- –mechanisms for hydrofracture genesis, growth, and healing;
- –relationships between matrix and fracture texture and permeability;
- –mass conservation of both fluid and solid;
- –grain scale and macroscopic force balance for fluid pressured porous media.

As these factors interact strongly, they must all be calculated simultaneously and self-consistently in order to capture the essence of the fluid-rock system at depth in the sedimentary basin.

We draw several conclusions about the nonlinear dynamics of fluids in sedimentary basins as a result of our study. Specifically we have found:

- –a transition occurs from an unfractured steady state to a state of oscillatory fluid release with increasing subsidence rate;

–a transition from an oscillatory state to a steady fractured state can occur in the early infilling of a sedimentary basin for intermediate burial rates;
–the tops of hydrofractured zones during the phase of steady-state fracturing remain at a fixed depth, between 2 and 3 km in our model, acting effectively as a front of hydrofracturing moving with respect to the rock-fixed frame of reference. This is characteristic only of the steady-fracturing behavior;
–a transition occurs with increasing lateral stress from an oscillatory state with little fracture healing, to oscillatory fracture growth and healing and finally on to an unfractured steady state;
–a strong degree of structuring is evident in the spatial distribution of fracture radii with depth, which suggests that similar distributions may be evident in nature, possibly in the form of spatial clusters of fluid inclusion trails, for example; and
–textural heterogeneity could exert a large influence on the evolution of fluid pressure at depth, and we suggest that the interaction of lithologies compacting at different rates can lead to a "stacking" of fluid compartments with depth.

Some general features of our model should be evident from field studies of seals and abnormally pressured fluid compartments in general. These include the spatial distribution of healed and unhealed fractures and the relative height of top seals as a function of burial rate, lateral basin constraint, and lithology. The distance between top and bottom seals may also decrease with increasing lateral stresses, which in basins will be strongly tied to the tectonic history but may also depend on basin size and morphology.

Many of the features brought out in the simple topological analysis presented in the first part of this paper are evident in the numerical simulations and aid in interpreting the results of the more complicated model. We suggest that despite its obvious simplicity, such an analysis is useful and can be thought of as a type of classification scheme for fluid compartment behavior.

By thinking of basin evolution in terms of coupled processes we can begin to link basin characteristics with basin history. This is a necessary step in understanding the evolution of abnormally pressured fluid compartments and their influence on basin hydrology.

## ACKNOWLEDGMENTS

Research supported by a contract with the Gas Research Institute (No. 5092-260-2443) and a grant from the Basic Energy Sciences Program of the U.S. Department of Energy (No. DEFG291ER14175).

## REFERENCES

Al-Shaieb, Z., Puckette, J., Ely, P., and Abdalla, A., 1991, The mega-compartment complex: Annual Report, February 1991, for the Gas Research Institute Project entitled Genesis of Basin Chambers and Sealing Structures, p. 3–69.

Angevine, C. L., and Turcotte, D. L., 1983, Porosity reduction by pressure solution: a theoretical model for quartz arenites: Geological Society of America Bulletin, v. 94, p. 1129–1134.

Atkinson, B. K., 1984, Subcritical crack growth in geological materials: Journal of Geophysical Research, v. 89, p. 4077–4114.

Baker, E. T., Lavelle, J. W., Feely, R. A., Massoth, G. J., and Walker, S. L., 1989, Episodic venting of hydrothermal fluids from the Juan de Fuca Ridge: Journal of Geophysical Research, v. 94, p. 9237–9250.

Barcilon, V., and Richter, F. M., 1986, Nonlinear waves in compacting media: Journal of Fluid Mechanics, v. 164, p. 429–448.

Bell, J. S., 1989, Vertical migration of hydrocarbons at Alma, offshore eastern Canada: Bulletin of Canadian Petroleum Geology, v. 37, p. 358–364.

Blot, M. A., and Willis, D. G., 1957, The elastic coefficients of the theory of consolidation: Journal of Applied Mechanics, v. 24, p. 594–601.

Bradley, J. S., 1975, Abnormal formation pressure: Bulletin of the American Association of Petroleum Geologists, v. 59, p. 957–973.

Brantley, S., Evans, B., Hickman, S. H., and Crerar, D. A., 1990, Healing of microcracks in quartz: Implications for fluid flow: Geology, v. 18, p. 136–139.

Brown, S. R., 1989, Transport of fluid and electric current through a single fracture: Journal of Geophysical Research, v. 94, p. 9429–9438.

Cathles, L. M., 1989, Overpressuring, episodic fluid flow, and process coupling in sedimentary basins [abstract]: EOS, p. 1097.

Cathles, L. M., and Smith, A. T., 1983, Thermal constraints on the formation of Mississippi Valley-type lead-zinc deposits and their implications for episodic basin dewatering and deposit genesis: Economic Geology, v. 78, p. 983–1002.

Chen, W., Ghaith, A., Park, A., and Ortoleva, P., 1990, Diagenesis through coupled processes: Modeling approach, self-organization and implications for exploration, *in* Meshri, I., and Ortoleva, P., editors, Prediction of Reservoir Quality through Chemical Modeling: American Association of Petroleum Geologists Memoir 49, p. 103–130.

Dewers, T., and Ortoleva, P., 1988, The role of geochemical self-organization in the migration and trapping of hydrocarbons: Applied Geochemistry, v. 3, p. 287–316.

———— 1990a, A coupled reaction/transport/mechanical model for intergranular pressure solution, stylolites, and differential compaction and cementation in clean sandstones: Geochimica et Cosmochimica Acta, v. 54, p. 1609–1625.

———— 1990b, The interaction of reaction, mass transport, and rock deformation during diagenesis: Mathematical modelling of intergranular pressure solution, stylolites, and differential compaction/cementation, *in* Meshri, I., and Ortoleva, P., editors, Prediction of Reservoir Quality through Chemical Modeling: American Association of Petroleum Geologists Memoir, p. 147–160.

———— 1994, Formation of stylolites, marl/limestone alternations, and clay seams accompanying chemical compaction of argillaceous carbonates, *in* Wolf, K. H. and Chilingarian, G. V., editors, Diagenesis, v. 1V: Amsterdam, Elsevier, p. 155–216.

Dickinson, G., 1953, Geological aspects of abnormal reservoir pressures in Gulf Coast Louisiana: American Association of Petroleum Geologists Bulletin, v. 37, p. 410–432.

Dieterich, J. H., 1989, Models of fault constitutive properties and earthquake occurrence: paper presented at SIAM Conference on Mathematical and Computational Issues in Geophysical Fluid and Solid Mechanics, Sept. 25–28, Houston, Texas.

Domenico, P. A., and Palciauskas, V. V., 1988, The generation and dissipation of abnormal fluid pressures in active depositional environments, *in* Back, W., Rosenshein, J. S., and Seaber, P. R., editors, Hydrogeology, The Geology of North America, v.O-2: Boulder, Colorado, Geological Society of America.

Dutton, R., 1974, The propagation of cracks by diffusion, *in* Bradt, R. C., Hasselman, D. P. H., and Lange, F. F., editors, Fracture Mechanics of Ceramics, v. 2: New York, Plenum, p. 649–657.

Engelder, T., and Scholz, C. H., 1981, Fluid flow along very smooth joints at effective pressures up to 200m megapascals, *in* Carter, N. L., Friedman, M., Logan, J. M., and Stearns, D. W., editors: Mechanical Behavior of Crustal Rocks: American Geophysical Union, Geophysical Monograph 24, p. 147–152.

Eshelby, J. D., 1957, The determination of the elastic field of an ellipsoidal inclusion and related problems: Proceedings of the Royal Society of London, Series A 241, p. 376–396.

Etheridge, M. A., Wall, V. J., and Vernon, R. H., 1983, The role of the fluid phase during regional metamorphism and deformation: Journal of Metamorphic Geology, v. 1, p. 205–226.

Feinn, D., and Ortoleva, P., 1977, Catastrophe and propagation in chemical reactions: Journal of Chemical Physics, v. 67, p. 2119.

Field, R. J., and Burger, M., 1985, Oscillations and Traveling Waves in Chemical Systems: New York, John Wiley & Sons, 681 p.

Freeze, R. A., and Cherry, J. A., 1979, Groundwater: Englewood Cliffs, New Jersey, Prentice-Hall, 604 p.

Ghaith, A., Chen, W., and Ortoleva, P., 1990, Oscillatory methane release from shale source rock, *in* Ortoleva, P., Hallet, B., McBirney, A., Meshri, I., Reeder, R., and Williams, P., editors, Self-Organization in Geological Systems, Proceedings of a Workshop held 26–30 June 1988, University of California, Santa Barbara: Earth Science Reviews, v. 29, p. 241–248.

Harrison, W. J., and Summa, L. L., 1991, Paleohydrology of the Gulf of Mexico Basin: American Journal of Science, v. 291, p. 109–176.

Houseknecht, D., 1988, Intergranular pressure solution in four quartzose sandstones: Journal of Sedimentary Petrology, v. 58, p. 228–246.

Hunt, J. M., 1990, Generation and migration of petroleum from abnormally pressured fluid compartments: Bulletin of the American Association of Petroleum Geologists, v. 74, p. 1–12.

Mandl, G. and Harkness, R. M., 1987, Hydrocarbon migration by hydraulic fracturing, *in* Jones, M. E., and Preston, R. M. F., editors: Deformation of Sediments and Sedimentary Rocks: Geological Society of London Special Publication 29, 39–53.

McGarr, A., 1988, On the state of lithospheric stress in the absence of applied tectonic forces, Journal of Geophysical Research, v. 93, 13,609–13,617.

Momper, J., 1978, Oil migration limitations suggested by geological and geochemical considerations, *in* Physical and Chemical Constraints on Petroleum Migration: American Association of Petroleum Geologists Continuing Education Course Notes, series 8, 23 p.

Nicolis, G. and Prigogine, I., 1977, Self-Organization in Non-Equilibrium Systems: From Dissipative Structures to Order through Fluctuations: New York, Wiley-Interscience, 491 p.

Ortoleva, P., 1990, Role of attachment kinetic feedback in the oscillatory zoning of crystals grown from melts, *in* Ortoleva, P., Hallet, B., McBirney, A., Meshri, I., Reeder, R., and Williams, P., editors: Self-Organization in Geological Systems, Proceedings of a Workshop held 26–30 June 1988, University of California Santa Barbara: Earth Science Reviews, v. 29, p. 3–8.

———— 1992, Nonlinear Chemical Waves: Chichester, John Wiley and Sons, 302 p.

———— 1993, Self-organization and nonlinear dynamics in sedimentary basins: Philosophical Transactions of the Royal Society of London, Series A 344, p. 171–179.

Ortoleva, P., Al-Shaieb, Z., and Puckette, J., in press. Genesis and dynamics of basin compartments and seals: American Journal of Science.

Ortoleva, P., Hallet, B., McBirney, A., Meshri, I., Reeder, R., and Williams, P., editors, 1990, Self-Organization in Geological Systems, Proceedings of a Workshop held 26–30 June 1988, University of California Santa Barbara: Earth Science Reviews, v. 29, 417 p.

Ortoleva, P., Merino, E., Chadam, J., and Moore, C. H., 1987, Geochemical self-organization I: feedback mechanisms and modeling approach: American Journal of Science, v. 287, p. 979–1007.

Ortoleva, P., and Ross, J., 1975, Theory of the propagation of discontinuities in kinetic systems with multiple time scales: fronts, front multiplicity, and pulses: Chemical Physics, v. 63, p. 3398.

Palciauskas, V. V., and Domenico, P. A., 1989, Fluid pressures in deforming porous rocks: Water Resources Research, v. 25, p. 203–213.

Pollard, D. D., and Aydin, A., 1988, Progress in understanding jointing over the past century: Geological Society of America Bulletin, v. 100, p. 1181–1204.

Powley, D., 1980, Normal and abnormal pressure: Lecture presented to American Association of Petroleum Geologists Advanced Exploration Schools, 1980–1987.

———— 1990, Pressures, hydrogeology and large scale seals in petroleum basins, *in* Ortoleva, P., Hallet, B., McBirney, A., Meshri, I., Reeder, R., and Williams, P., editors: Self-organization in Geological Systems, Proceedings of a Workshop held 26–30 June 1988, University of California Santa Barbara: Earth Science Reviews, v. 29, p. 215–226.

Prikryl, J. D., Posey, H., and Kyle, J. R., 1988, A petrographic and geochemical model for the origin of calcite cap rock at Damon Mound Salt Dome, Texas, U.S.A.: Chemical Geology, v. 74, p. 67–97.

Rice, J. R., and Bolsvert, R. F., 1985, Solving Elliptic Problems Using ELLPACK: New York, Springer-Verlag, 497 p.

Rice, J. R., and Rudnicki, J. W., 1979, Earthquake precursor effects due to pore fluid stabilization of a weakening fault zone: Journal of Geophysical Research, v. 84, p. 2177–2193.

Scheidegger, A. E., 1974, The Physics of Flow Through Porous Media: University of Toronto Press, 353 p.
Schmidt, V., and McDonald, D. A., 1979, The role of secondary porosity in the course of sandstone diagenesis, *in* Scholle, P. A., and Schulger, P. R., editors: Aspects of Diagenesis, Society of Economic Paleontologists and Mineralogists Special Publication 26, p. 175–207.
Segall, P., 1984, Rate-dependent extensional deformation resulting from crack growth in rock: Journal of Geophysical Research, v. 89, p. 4185–4195.
Smith, D. L., and Evans, B., 1984, Diffusional crack healing in quartz: Journal of Geophysical Research, v. 89, p. 4125–4135.
Swanson, P. L., 1984, Subcritical crack growth and other time- and environment-dependent behavior in crustal rocks: Journal of Geophysical Research, v. 89, p. 4137–4152.
Tada, R., Maliva, R., and Siever, R., 1987, A new mechanism for pressure solution in porous quartzose sandstone: Geochimica et Cosmochimica Acta, v. 51, p. 2295–2301.
Tada, R., and Siever, R., 1989, Pressure solution during diagenesis: A review: Annual Review of Earth Planetary Sciences, v. 17, p. 89–118.
Tigert, V., and Al-Shaieb, Z., 1990, Pressure seals: their diagenetic banding patterns: *in* Ortoleva, P., Hallet, B., McBirney, A., Meshri, I., Reeder, R., and Williams, P., editors: Self-Organization in Geological Systems, Proceedings of a Workshop held 26–30 June 1988, University of California Santa Barbara: Earth Science Reviews, v. 29, p. 227–240.
Ungerer, P., Burrus, J., Doligez, B., Chenet, P. Y., and Bessis, F., 1990, Basin evaluation by integrated two-dimensional modeling of heat transfer, fluid flow, hydrocarbon generation, and migration: Bulletin of the American Association of Petroleum Geologists, v. 74, p. 309–335.
Walder, J., and Nur, A., 1984, Porosity reduction and crystal pore pressure development: Journal of Geophysical Research, v. 89, p. 11,539–11,548.
Walsh, J. B., 1965, The effect of cracks on the compressibility of rock: Journal of Geophysical Research, v. 70, p. 381–389.
Walsh, J. B., and Brace, W. F., 1984, The effect of pressure on porosity and the transport properties of rock: Journal of Geophysical Research, v. 89, p. 9425–9431.
Wang, J. S. Y., Tsang, C. F., and Sternbentz, R. A., 1983, The state of the art of numerical modeling of thermohydrologic flow in fractured rock masses: Environmental Geology, v. 4, p. 133–199.
Weedman, S. D., Guber, A. L., and Engelder, T., 1992, Pore pressure variation within the Tuscaloosa Trend: Morganza and Moore-Sams Fields, Louisiana Gulf Coast: Journal of Geophysical Research, v. 97, p. 7193–7202.
Weyl, P. K., 1959, Pressure solution and the force of crystallization—a phenomenological theory: Journal of Geophysical Research, v. 64, p. 2001–2025.
Zeeman, E. C., 1972, *in* Towards a Theoretical Biology, 4: Chicago, Aldine-Atherton, p. 8.
Zimmerman, R. W., Haraden, J. L., and Somerton, W. H., 1985, The effects of pore pressure and confining pressure on pore and bulk volume compressibilities of consolidated sandstones, *in* Pincus, H. J. and Hoskins, E. R., editors: Measurement of Rock Properties at Elevated Pressures and Temperatures, ASTM STP 869: Philadelphia, American Society for Testing and Materials, p. 24–36.